(Preprint) AAS 25-100

PERFORMANCE IMPACTS TO THE NASA ARTEMIS II TRAJECTORY CORRECTION BURN PLACEMENT

David Woffinden[*], Benjamin Margolis[†], Shane Robinson[‡]

As NASA embarks to return humans to the lunar vicinity with the upcoming Artemis II mission, the selected free return trajectory taking the crew to the Moon in the Orion spacecraft is impacted by the execution of small trajectory correction burns to ensure the spacecraft stays on course for a successful return to Earth. The placement of these nominally zero translational maneuvers must account for the crew schedule, navigation tracking constraints, spacecraft venting, thermal and communication requirements, and a host of other programmatic factors. Understanding the influence the placement of these periodic burn corrections have on the integrated GN&C performance can provide valuable insight to mission controllers and trajectory planning processes to untangle the complex trade space considered for both baseline and contingency scenarios. This sensitivity information can also be utilized to facilitate the optimized placement of these burns. This paper utilizes several techniques to systematically generate the performance impacts to the NASA Artemis II trajectory correction burn placement and demonstrate how to derive optimized locations that make the system robust to crew activity, maneuver execution errors, navigation uncertainty, orbit insertion errors, disturbance accelerations, and other system limitations.

INTRODUCTION

The upcoming NASA Artemis missions represent a significant step in returning humans to the lunar surface and other exploration destinations. As depicted in Figure 1, the Artemis II mission is the next step on this journey. It utilizes a free-return trajectory that is reminiscent of the Apollo 8 mission and relies on periodic trajectory corrections following the trans-lunar injection (TLI) burn to ensure the crew returns safely to Earth. The placement of these nominally zero translational maneuvers must account for the crew schedule, navigation tracking constraints, spacecraft venting, thermal and communication requirements, and a host of other programmatic factors. Understanding the influence the placement of these periodic burn corrections have on the integrated GN&C performance can provide valuable insight to mission controllers and trajectory planning processes to untangle the complex trade space considered for both baseline and contingency scenarios. This sensitivity information can also be utilized to facilitate the prudent placement of these burns.

A previous study investigated the optimized placement of these trajectory correction burns that accounted for uncertainty in the system, the dynamics of the cis-lunar transfer, the geometry of the utilized sensor measurements from the ground tracking stations of the primary navigation system along with the geometry of the Earth and Moon for the backup optical navigation system, the crew

[*] Aerospace Engineer, GN&C Autonomous Flight Systems Branch, NASA Johnson Space Center, Houston TX, 77058
[†] Aerospace Engineer, NASA Ames Research Center, Moffett Field, CA, 94035
[‡] Aerospace Engineer, GN&C Autonomous Flight Systems Branch, NASA Johnson Space Center, Houston TX, 77058

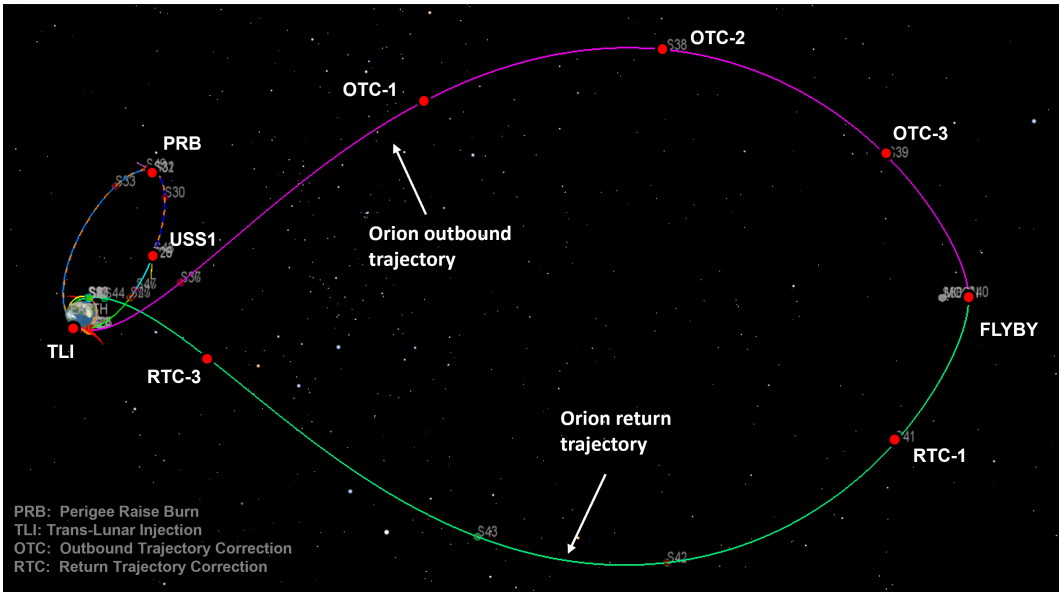

Figure 1. Notional Orion Free-Return Trajectory for the NASA Artemis II Mission

schedule, spacecraft venting, targeting and burn plan configurations, thruster selection, and the complex interaction of the overall integrated guidance, navigation, and control (GN&C) system. Robust trajectory optimization techniques were adopted to solve this comprehensive problem which utilized a linear covariance (LinCov) analysis[1,2] tool interfaced with a genetic algorithm (GA).[3,4,5,6,7,8,9] The objective was to minimize the total 3-sigma delta-v usage while constraining the entry interface trajectory dispersions to remain within the allocated performance specifications.

This paper intends to build off this earlier analysis by highlighting the sensitivity of the placement of the trajectory correction burn placement to the key performance metrics such as entry interface dispersions and total delta-v in the form of mission maps.[10] These mission maps can provide valuable insight to mission controllers and the trajectory planning processes to untangle the complex trade space considered for both baseline and contingency scenarios. With the trends extracted from the mission maps, a simple demonstration is made how the optimized burn placement for the final return trajectory correction burn can be identified manually for several different objective functions. These intuitively derived solutions available to a mission planner and trajectory operator are confirmed using a gradient-based optimization technique to systematically derive optimized locations that make the system robust to crew activity, venting, maneuver execution errors, navigation uncertainty, orbit insertion errors, disturbance accelerations, and other system limitations. Although the approach is different, the objective still remains the same of generating sensitivity data to key performance metrics (such as total delta-v usage and trajectory dispersions) to identify the optimal location of the outbound and return trajectory correction burns.

ANALYSIS APPROACH

Performance Metrics

To quantify the impacts of the trajectory correction burns placements to the Artemis II integrated GN&C performance, there are several performance metrics that are utilized which include

the true trajectory dispersions $\delta\mathbf{x}$, the navigation dispersions $\delta\hat{\mathbf{x}}$, the true navigation error $\delta\mathbf{e}$, and the onboard navigation error $\delta\hat{\mathbf{e}}$ as depicted in Figure 2. The true dispersions $\delta\mathbf{x}$ are defined as the

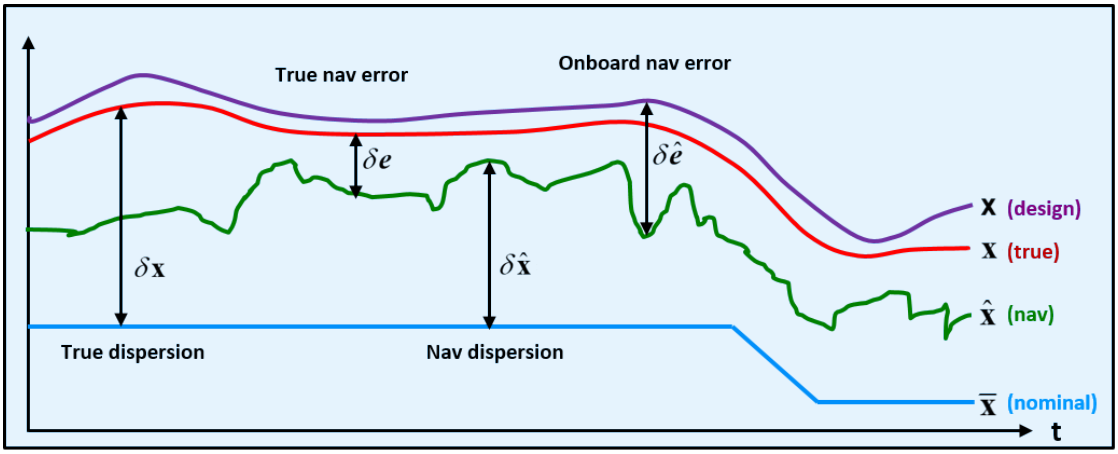

Figure 2. GN&C Performance Metric Variables

difference between the true state $\mathbf{x}$ and the nominal state $\bar{\mathbf{x}}$. The true state $\mathbf{x}$ is an n-dimensional vector that represents the *real world* environment or actual state.

$$\delta\mathbf{x} \triangleq \mathbf{x} - \bar{\mathbf{x}} \qquad\qquad \mathbf{D} = E\left[\delta\mathbf{x}\delta\mathbf{x}^{\mathrm{T}}\right] \tag{1}$$

The nominal state $\bar{\mathbf{x}}$ is also an n-dimensional vector that represents the desired or reference state. The covariance of the environment dispersions, $\mathbf{D}$, indicates how precisely the system can follow a desired trajectory.

The navigation dispersions $\delta\hat{\mathbf{x}}$ are defined as the difference between the navigation state $\hat{\mathbf{x}}$ and the nominal state $\bar{\mathbf{x}}$. The navigation state is an $\hat{n}$-dimensional vector ($\hat{n} < n$) that represents the filter's estimated state.

$$\delta\hat{\mathbf{x}} \triangleq \hat{\mathbf{x}} - \mathbf{M}_x\bar{\mathbf{x}} \qquad\qquad \hat{\mathbf{D}} = E\left[\delta\hat{\mathbf{x}}\delta\hat{\mathbf{x}}^{\mathrm{T}}\right] \tag{2}$$

The matrix $\mathbf{M}_x$ is an $(\hat{n} \times n)$ matrix that maps the estimated state in terms of the true and nominal state. The covariance of the navigation dispersions, $\hat{\mathbf{D}}$, reflect how precisely the onboard system thinks it can follow a prescribed reference trajectory.

The true navigation error $\delta\mathbf{e}$ is the difference between the environment and navigation states. It is also the difference between the environment and the navigation dispersions.

$$\delta\mathbf{e} \triangleq \mathbf{M}_x\mathbf{x} - \hat{\mathbf{x}} = \mathbf{M}_x\delta\mathbf{x} - \delta\hat{\mathbf{x}} \qquad\qquad \mathbf{P} = E\left[\delta\mathbf{e}\delta\mathbf{e}^{\mathrm{T}}\right] \tag{3}$$

The covariance of the true navigation error, $\mathbf{P}$, quantifies how precisely the onboard navigation system can estimate the actual state.

The onboard navigation error $\delta\hat{\mathbf{e}}$ itself is never computed, but it is used to develop the onboard navigation filter equations. It is defined as the difference between the design state, x, and the navigation state $\hat{\mathbf{x}}$.

$$\delta\hat{\mathbf{e}} \triangleq \mathrm{x} - \hat{\mathbf{x}} \qquad\qquad \hat{\mathbf{P}} = E\left[\delta\hat{\mathbf{e}}\delta\hat{\mathbf{e}}^{\mathrm{T}}\right] \tag{4}$$

The covariance of the onboard navigation error, $\hat{\mathbf{P}}$, quantifies how precisely the onboard navigation system expects it can determine the actual state. The performance of the onboard navigation system is determined by comparing $\hat{\mathbf{P}}$ to the actual navigation performance $\mathbf{P}$. If the *true* states and the *design* states are assumed to be the same, then the true navigation covariance will equal the onboard navigation covariance.

The covariances of the true dispersions, navigation dispersions, true navigation error, and the onboard navigation error are ultimately used to analyze and assess the performance of a proposed GN&C system. A common approach to obtain these performance metrics is to use a Monte Carlo simulation outlined in Figure 3, where the sample statistics of hundreds or thousands of runs, N, are used to numerically compute the desired covariance matrices.

$$\mathbf{D} = \frac{1}{N-1}\sum \delta\mathbf{x}\delta\mathbf{x}^{\mathrm{T}} \qquad \hat{\mathbf{D}} = \frac{1}{N-1}\sum \delta\hat{\mathbf{x}}\delta\hat{\mathbf{x}}^{\mathrm{T}} \qquad \mathbf{P} = \frac{1}{N-1}\sum \delta\mathbf{e}\delta\mathbf{e}^{\mathrm{T}} \tag{5}$$

The onboard navigation error covariance $\hat{\mathbf{P}}$ is the navigation filter covariance for each run. This same statistical information can be obtained using linear covariance analysis techniques.

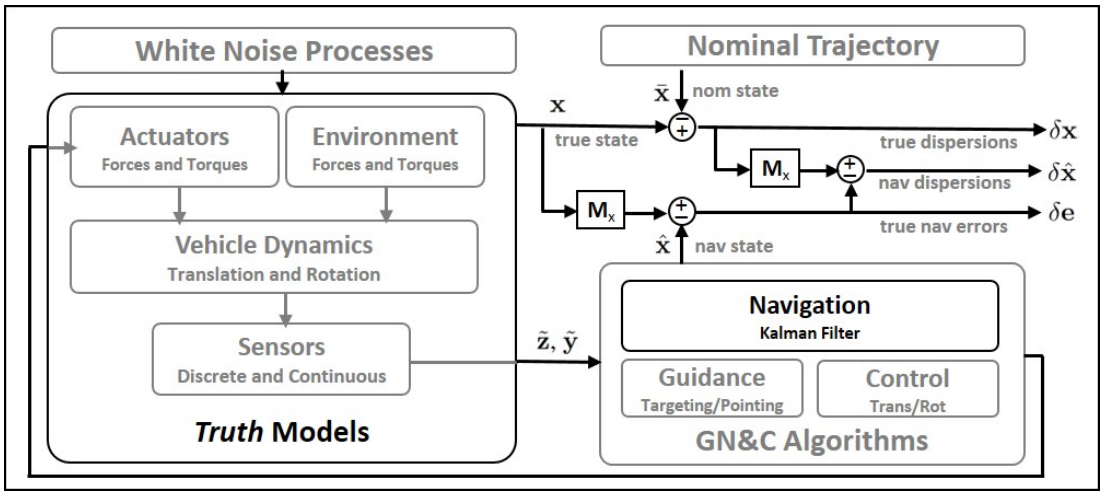

Figure 3. Extracting GN&C Performance Metrics Using Monte Carlo Techniques

Linear covariance analysis incorporates the non-linear system dynamics models and GN&C algorithms to generate a nominal reference trajectory $\bar{\mathbf{x}}$ which is then used to propagate, update, and correct an onboard navigation covariance matrix $\hat{\mathbf{P}}$ and an augmented state covariance matrix $\mathbf{C}$,

$$\mathbf{C} = E\left[\delta\mathbf{X}\delta\mathbf{X}^{\mathrm{T}}\right] \tag{6}$$

where the augmented state $\delta\mathbf{X}^{\mathrm{T}} = [\delta\mathbf{x}^{\mathrm{T}}\ \delta\hat{\mathbf{x}}^{\mathrm{T}}]$ consists of the true dispersions and the navigation dispersions. Pre- and post-multiplying the augmented state covariance matrix by the following mapping matrices, the covariances for the trajectory dispersions, navigation dispersions, and the navigation error can be obtained.

$$\begin{aligned}
\mathbf{D} &= [\,\mathbf{I}_{n\times n},\ \mathbf{0}_{n\times\hat{n}}\,]\,\mathbf{C}\,[\,\mathbf{I}_{n\times n},\ \mathbf{0}_{n\times\hat{n}}\,]^{\mathrm{T}} \\
\hat{\mathbf{D}} &= [\,\mathbf{0}_{\hat{n}\times n},\ \mathbf{I}_{\hat{n}\times\hat{n}}\,]\,\mathbf{C}\,[\,\mathbf{0}_{\hat{n}\times n},\ \mathbf{I}_{\hat{n}\times\hat{n}}\,]^{\mathrm{T}} \\
\mathbf{P} &= [\,\mathbf{I}_{\hat{n}\times n},\ -\mathbf{I}_{\hat{n}\times\hat{n}}\,]\,\mathbf{C}\,[\,\mathbf{I}_{\hat{n}\times n},\ -\mathbf{I}_{\hat{n}\times\hat{n}}\,]^{\mathrm{T}}
\end{aligned} \tag{7}$$

Linear Covariance Analysis

The linear covariance analysis equations used to propagate, update, and correct both the augmented state covariance matrix and the onboard navigation covariance matrix are summarized here along with the LinCov analysis inputs. For additional details regarding the development and implementation of the linear covariance simulation, see the following references.[1, 2, 11, 12, 13, 14]

LinCov Analysis Modeling The discrete-time propagation equations for augmented state covariance matrix $\mathbf{C}$ and the onboard navigation covariance matrix $\hat{\mathbf{P}}$ are

$$\mathbf{C}(t_{k+1}) = \mathbf{\Phi}(t_{k+1}, t_k)\mathbf{C}(t_k)\mathbf{\Phi}^T(t_{k+1}, t_k) + \mathbf{G}\mathbf{Q}\mathbf{G}^T \tag{8}$$

$$\hat{\mathbf{P}}(t_{k+1}) = \hat{\mathbf{\Phi}}(t_{k+1}, t_k)\hat{\mathbf{P}}(t_k)\hat{\mathbf{\Phi}}^T(t_{k+1}, t_k) + \hat{\mathbf{G}}\hat{\mathbf{Q}}\hat{\mathbf{G}}^T \tag{9}$$

where $\mathbf{\Phi}$ and $\hat{\mathbf{\Phi}}$ are augmented and onboard state transition matrices respectively for the linearized perturbation dynamics about the reference trajectory. The mapping matrices, $\mathbf{G}$ and $\hat{\mathbf{G}}$, are used to map environmental and navigation process noise characterized by $\mathbf{Q}$ and $\hat{\mathbf{Q}}$, into $\mathbf{C}$ and $\hat{\mathbf{P}}$.

The measurement update equations for augmented and navigation state covariance matrices, $\mathbf{C}$ and $\hat{\mathbf{P}}$, at a measurement time t_i are

$$\mathbf{C}^+(t_i) = \mathbf{A}\mathbf{C}^-(t_i)\mathbf{A}^T + \mathbf{B}\mathbf{R}^j(t_i)\mathbf{B}^T \tag{10}$$

$$\hat{\mathbf{P}}^+(t_i) = \left[\hat{\mathbf{I}} - \hat{\mathbf{K}}^j(t_i)\hat{\mathbf{H}}^j\right]\hat{\mathbf{P}}^-(t_i)\left[I - \hat{\mathbf{K}}^j(t_i)\hat{\mathbf{H}}^j\right]^T + \hat{\mathbf{K}}^j(t_i)\hat{\mathbf{R}}^j(t_i)\hat{\mathbf{K}}^j(t_i)^T \tag{11}$$

where the superscript 'j' denotes the jth measurement type. The Kalman gain is written as

$$\hat{\mathbf{K}}^j(t_i) = \hat{\mathbf{P}}(t_i)(\hat{\mathbf{H}}^j)^T\left[\hat{\mathbf{H}}^j\hat{\mathbf{P}}^-(t_i)(\hat{\mathbf{H}}^j)^T + \hat{\mathbf{R}}^j(t_i)\right]^{-1} \tag{12}$$

The matrices $\hat{\mathbf{H}}$ and $\hat{\mathbf{R}}$ are the measurement sensitivity and measurement noise matrices respectively. The matrices $\mathbf{A}$ are $\mathbf{B}$ map the effects of the measurements and their associated noise to the navigation state dispersions.

The correction equations for $\mathbf{C}$ and $\hat{\mathbf{P}}$ at a maneuver time t_m are

$$\mathbf{C}^+(t_m) = \mathbf{M}\mathbf{C}^-(t_m)\mathbf{M}^T + \mathbf{N}\boldsymbol{Q}_w^{act}\mathbf{N}^T \tag{13}$$

$$\hat{\mathbf{P}}^+(t_m) = \left[\hat{\mathbf{I}} + \hat{\mathbf{M}}\right]\hat{\mathbf{P}}^-(t_m)\left[I + \hat{\mathbf{M}}\right]^T + \hat{\mathbf{N}}\hat{\mathbf{Q}}_w^{act}\hat{\mathbf{N}}^T \tag{14}$$

The matrices $\mathbf{M}$ and $\hat{\mathbf{M}}$ contain the control partials associated with targeting algorithm. The matrices $\mathbf{N}$ and $\hat{\mathbf{N}}$ are used to map the effects of actuator noise, described by $\boldsymbol{Q}_w^{act}$ and $\hat{\mathbf{Q}}_w^{act}$, into $\mathbf{C}$ and $\hat{\mathbf{P}}$.

GN&C MODELING

Following the trans-lunar injection (TLI) burn, the subsequent outbound trajectory correction (OTC) burns and the return trajectory correction (RTC) burns are nominally zero for the Artemis II free-return profile, regardless of when they are executed. The placement of the OTC and RTC burns do not impact the nominal performance, but they can have a significant influence on the integrated GN&C results when uncertainty in the system is included. Consequently, the optimization of the timing of the trajectory correction burns is driven by the implementation of the vehicle's GN&C

system in context of the baseline Artemis II reference trajectory, the operational and crew time line, navigation modes, target configurations and burn plans, along with venting and disturbance acceleration modeling. This section contains the GN&C modeling assumptions and parameter specification that influences the burn placement impact.

Notional Artemis II Trajectory Profile and Time Line

An overview of the notional Artemis II trajectory profile is provided in Figure 4 where Figure 4(a) highlights the trajectory in the Earth/Moon rotating frame and Figure 4(b) shows the altitude profile as a function of time along with a notional scheduling of the sensor measurements. The solid blue line represents the nominal reference trajectory with the solid red dots indicating major events such as translational burns. The thick black lines mark the designated crew sleep periods which consists of the pre-sleep, actual sleep, and post-sleep allocations.

The scenario depicted starts in Earth orbit following an initial apogee raise burn (ARB) just 61 minutes prior to the upper stage separation (USS2) burn. Following USS2 and during the first crew sleep period, the perigee raise burn (PRB) is performed which is about 12 hours prior to the trans-lunar injection (TLI) burn. TLI places Orion on a free-return trajectory that does a flyby of the moon about 4 days later and ultimately returns back to earth approximately 8 days following TLI. Twenty-four hours after TLI, the first outbound trajectory correction burn (OTC1) is scheduled. The baseline time line places the second OTC burn (OTC2) 24 hours after OTC1 and the third OTC burn (OTC3) is assumed to occur 24 hours prior to lunar flyby while avoiding the actual crew sleep period. As Orion begins its journey home, the first return trajectory correction burn (RTC1) is performed one day after lunar flyby. The last two return trajectory correction burns, RTC2 and RTC3, are executed both 21 hours and 5 hours prior to entry interface respectively. A summary of the timeline is provided in Table 1.

Table 1. Baseline Artemis II Time Line, Targeting, and Sensor Utilization

Event	Description	MET	Targ	Sensors
START	Post Apogee Raise Burn	0:00:00:00	—-	IMU, Startracker, DSN, GPS
USS2	Upper Stage Separation Burn	0:01:01:00	TLT	IMU, Startracker, DSN
PRB	Perigee Raise Burn	0:09:45:23	TLT	IMU, Startracker, DSN
TLI	Trans-Lunar Injection Burn	0:21:32:56	TLT	IMU, Startracker, DSN, GPS
OTC1	Outbound Correction Burn #1	1:21:32:56	TLT	IMU, Startracker, DSN
OTC2	Outbound Correction Burn #2	2:21:32:56	TLT	IMU, Startracker, DSN (or OPNAV)
OTC3	Outbound Correction Burn #3	4:05:13:37	TLT	IMU, Startracker, DSN (or OPNAV)
FLYBY	Lunar Flyby	5:05:13:37	TLT	IMU, Startracker, DSN (or OPNAV)
RTC1	Return Correction Burn #1	6:03:13:37	TLT	IMU, Startracker, DSN (or OPNAV)
RTC2	Return Correction Burn #2	8:01:47:44	TLT	IMU, Startracker, DSN (or OPNAV)
RTC3	Return Correction Burn #3	8:17:47:44	TLT	IMU, Startracker, DSN (or OPNAV)
EI	Entry Interface	8:22:47:44	—-	IMU, Startracker, DSN, GPS

As illustrated in Figure 4(b), from the initial USS2 burn through TLI, it is assumed that Orion is able to use a baseline navigation configuration which consists of IMU, startracker, GPS, and Deep Space Network (DSN) or NASA Near Space Network (NSN) ground tracking updates. When

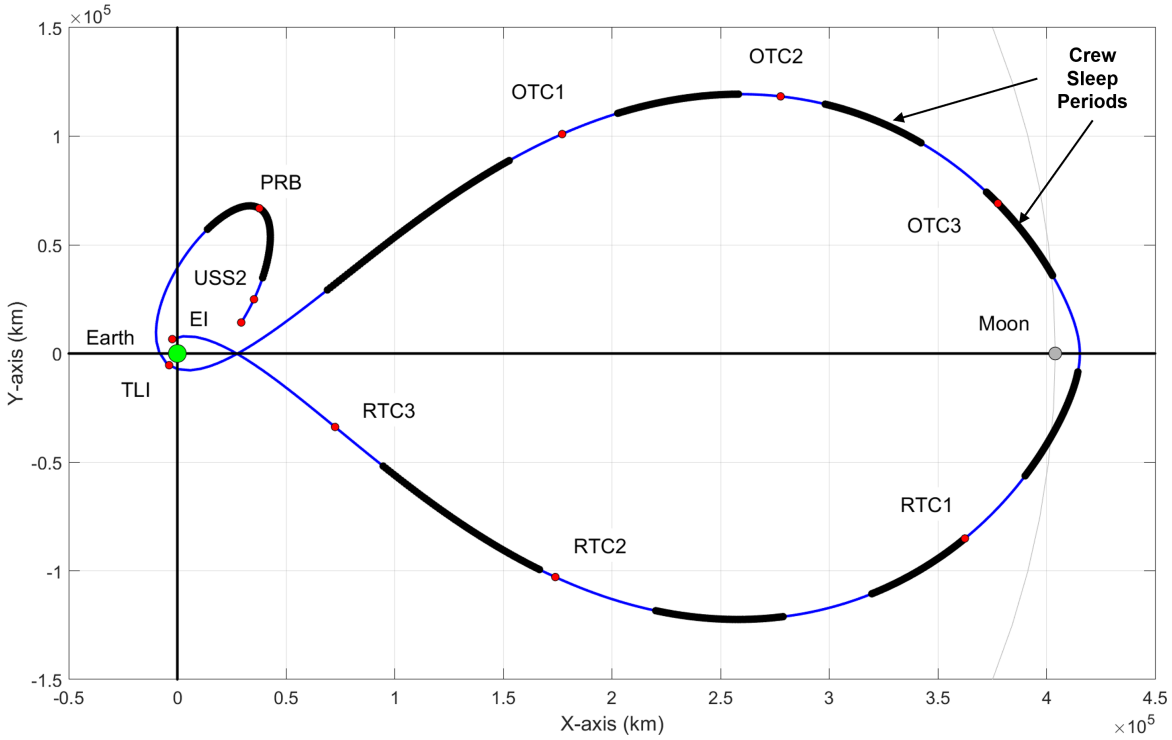

(a) Notional Artemis II trajectory overview in the Earth/Moon rotating frame with the baseline burn placement.

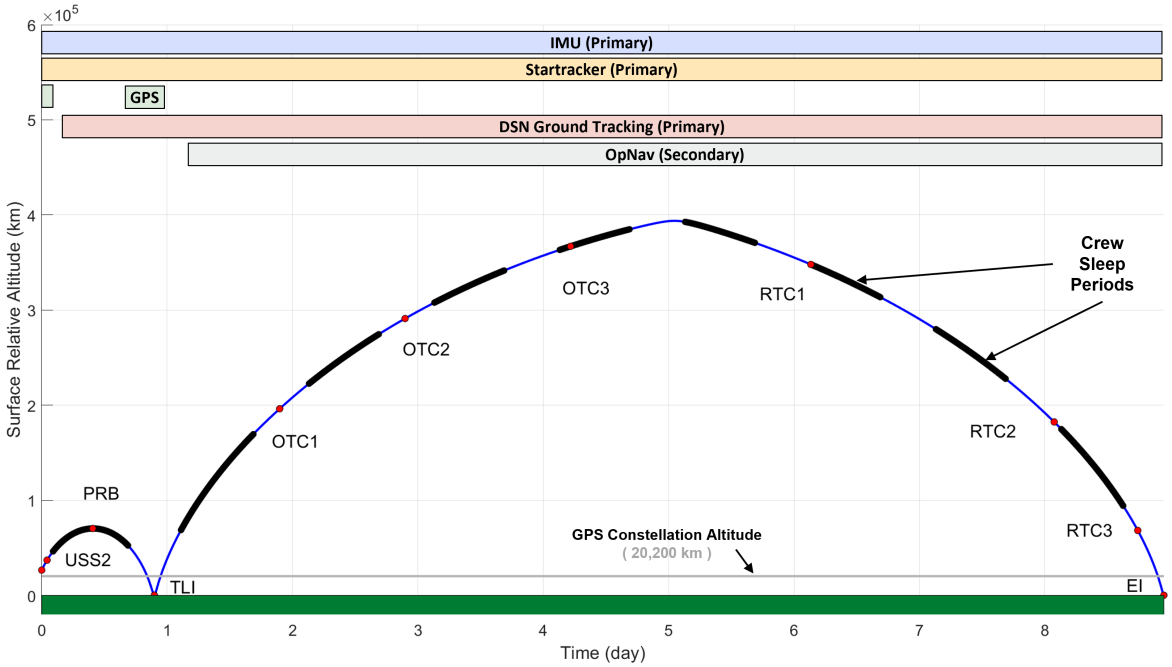

(b) Notional Artemis II altitude profile and sensor utilization

Figure 4. Notional Orion Artemis II Concept of Operations

Orion's altitude is within the GPS constellation, GPS measurements are processed. Following OTC1, either the primary DSN ground tracking system or the secondary backup optical navigation (OpNav) system can be utilized to support the subsequent trajectory correction burns. In general, prior to each burn and afterwards, either a DSN ground estimate is uplinked to the spacecraft to support targeting and burn execution or an optical navigation (OpNav) pass is performed. To generate the mission maps that illustrate the sensitivity of the placement of the correction burns, the simulation epoch will be one hour following TLI. Then each correction burn time for OTC1 through RTC3 are individually shifted at equal time intervals throughout the crew day that they are currently scheduled to be performed.

Notional Artemis II Top-Level Performance Requirements

For the Artemis II mission, top-level requirements exist to ensure the Orion spacecraft safely flies by the moon and returns the crew safely to Earth using the allocated propellant. For this analysis, the Orion spacecraft is to utilize less than 10 m/s of total delta-v for the outbound and return trajectory correction burns, and comply with the entry interface (EI) conditions that constrain the downtrack position, inertial velocity magnitude, inertial flight path angle, cross-track position, and cross-track velocity dispersions.[15,16,17,18] Failure to comply with these EI requirements will impact the probability of mission success. A summary of these top-level constraints adopted for nominal Artemis II operations are illustrated in Figure 5 for the 3-sigma dispersions.

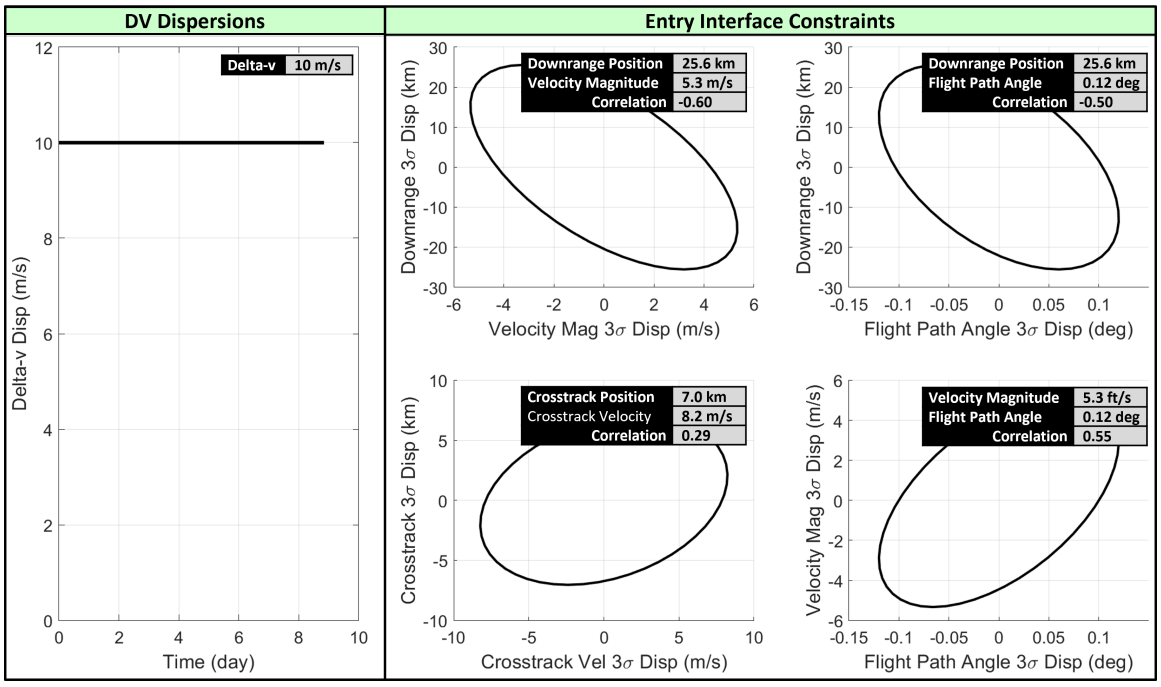

Figure 5. Notional Artemis II Correction Delta-v Dispersions and Entry Interface Constraints

Navigation System Modeling

Orion has both a primary and backup navigation system. The primary navigation system consists of The Deep Space Network (DSN) ground updates, accelerometers, gyros, star trackers, and GPS

measurements. The backup navigation system accounts for a loss of communication by replacing DSN with an with an onboard optical navigation (OpNav) system. Only the baseline navigation system is modeled for the trajectory correction burn placement analysis, but different fidelity navigation models of the primary system are highlighted. The mathematical equations used for the different measurement types are provided below.

DSN Ground Update The DSN ground update provides a position and velocity state estimate and covariance to the Orion vehicle at designated epochs based on range $\tilde{\rho}$ and doppler measurements $\tilde{\dot{\rho}}$ between the ground tracking station and the spacecraft which are functions of the spacecraft's inertial position $\mathbf{r}_l^i$, the mounted antenna location $\mathbf{r}_a^b$, spacecraft's inertial-to-body transformation matrix $\mathbf{T}_b^i$, the spacecraft's angular rate $\boldsymbol{\omega}_l^b$, the inertial-to-planet transformation $\mathbf{T}_p^i$, the Earth's angular rate $\boldsymbol{\omega}_e^p$, the ground station location $\mathbf{r}_{gs}^p$ in the planet-fixed frame, the range bias $\boldsymbol{b}_\rho$, doppler bias $\boldsymbol{b}_{\dot{\rho}}$, range noise $\boldsymbol{\upsilon}_\rho$, and doppler noise $\boldsymbol{\upsilon}_{\dot{\rho}}$.

$$\tilde{\rho} = \left|\mathbf{r}_l^i + \mathbf{T}_b^i \mathbf{r}_a^b - \mathbf{T}_p^i \mathbf{r}_{gs}^p\right| + \boldsymbol{b}_\rho + \boldsymbol{\upsilon}_\rho \tag{15}$$

$$\tilde{\dot{\rho}} = \frac{\left[\mathbf{v}_l^i + \mathbf{T}_b^i\left(\boldsymbol{\omega}_l^b \times \mathbf{r}_a^b\right) - \mathbf{T}_p^i\left(\boldsymbol{\omega}_e^p \times \mathbf{r}_{gs}^p\right)\right]^{\mathrm{T}}\left[\mathbf{r}_l^i + \mathbf{T}_b^i \mathbf{r}_a^b - \mathbf{T}_p^i \mathbf{r}_{gs}^p\right]}{\left[\mathbf{r}^i + \mathbf{T}_b^i \mathbf{r}_a^b - \mathbf{T}_p^i \mathbf{r}_{gs}^p\right]} + \boldsymbol{b}_{\dot{\rho}} + \boldsymbol{\upsilon}_{\dot{\rho}} \tag{16}$$

Three models are used to capture the performance of these periodic ground state updates (GSU). The first approach is a higher fidelity model that incorporates the selected ground stations, scheduling, switching logic, available measurement types and accuracies, vehicle disturbance accelerations, burn execution error, and an assortment of other details such as atmospheric impacts.[19,20] Three-way doppler measurements with six ground stations (both DSN and NSN ground stations) included.

To reduce the simulation burden and assess the sensitivity of delta-v and EI dispersion performance to navigation performance, two additional models with reduced computation cost and conservative navigation performance prediction are utilized. The first of these models is BLACMAGIC (Batch Like Approximate Covariance for the Modeling of Artemis Ground Induced Commands).[21] It provides a low-cost approximation for the covariances of a DSN-informed filtering solution. To reduce the simulation burden, BLACMAGIC has no time propagation of vehicle states, covariances, or observer locations and no measurement buffering, processing or generation. It simply generates an approximation of the state information contained in a set of DSN measurements. The third option for capturing the GSUs is adopting pregenerated covariance data that are uplinked to the vehicle based on conservative performance factors. The uncertainty parameters used for the DSN ground updates are given in Table 2.

Accelerometer The accelerometer measures the non-gravitational acceleration in the IMU case frame $\tilde{\mathbf{a}}^{imu}$, which is a function of the nominal inertial-to-body transformation matrix $\bar{\mathbf{T}}_i^b$, the nominal body-to-IMU transformation $\bar{\mathbf{T}}_b^{imu}$, the actual attitude dispersion $\boldsymbol{\theta}$, the misalignment $\boldsymbol{\mu}_a$, the constant scale factor $\mathbf{s}_a$, the Markov scale factor $\boldsymbol{\sigma}_a$, the constant bias $\mathbf{b}_a$, the Markov bias $\boldsymbol{\beta}_a$, the nonorthogonality factor $\boldsymbol{\gamma}_a$, and the velocity random walk (noise) $\boldsymbol{\upsilon}_a$.

$$\tilde{\mathbf{a}}^{imu} = \left(\mathbf{I} + [(\mathbf{s}_a + \boldsymbol{\sigma}_a)\diagdown]\right)\left[\left(\mathbf{I} + [\boldsymbol{\mu}_a\times]\right)\left(\mathbf{I} + [\boldsymbol{\gamma}_a *]\right)\bar{\mathbf{T}}_b^{imu}\left(\mathbf{I} + [\boldsymbol{\theta}\times]\right)\bar{\mathbf{T}}_i^b \mathbf{a}^i + \mathbf{b}_a + \boldsymbol{\beta}_a + \boldsymbol{\upsilon}_a\right] \tag{17}$$

The uncertainty parameters used for the accelerometer are listed in Table 3.

Gyro The gyros measure the vehicle's angular rates in the IMU case frame $\tilde{\boldsymbol{\omega}}^{imu}$ and is represented as a function of the nominal body-to-IMU transformation $\bar{\mathbf{T}}_b^{imu}$ where b indicates the vehicle body-fixed frame, the misalignment $\boldsymbol{\mu}_\omega$, the constant scale factor $\mathbf{s}_\omega$, the Markov scale factor $\boldsymbol{\sigma}_\omega$, the constant bias $\mathbf{b}_\omega$, the Markov bias $\boldsymbol{\beta}_\omega$, the nonorthogonality factor $\boldsymbol{\gamma}_\omega$, and the angular random walk (noise) $\boldsymbol{\upsilon}_\omega$

$$\tilde{\boldsymbol{\omega}}^{imu} = (\mathbf{I} + [(\mathbf{s}_\omega + \boldsymbol{\sigma}_\omega)\diagdown]) \left[(\mathbf{I} + [\boldsymbol{\mu}_\omega \times]) (\mathbf{I} + [\boldsymbol{\gamma}_\omega *]) \bar{\mathbf{T}}_b^{imu} \boldsymbol{\omega}^b + \mathbf{b}_\omega + \boldsymbol{\beta}_\omega + \boldsymbol{\upsilon}_\omega \right] \tag{18}$$

The uncertainty parameters used for the gyroscope are listed in Table 4.

Star Tracker The star tracker provides an accurate measurement of the vehicle's orientation. The generated inertial-to-star tracker quaternion is a function of the body-to-star tracker mounting $\mathbf{q}_b^{st}$, the actual inertial-to-body quaternion $\mathbf{q}_i^b$, the sensor bias $\mathbf{b}_{st}$, noise $\boldsymbol{\eta}_{st}$, and misalignment $\boldsymbol{\mu}_{st}$

$$\tilde{\mathbf{q}}_{st}^i = \mathbf{q}(\boldsymbol{\eta}_{st}) \otimes \mathbf{q}(\mathbf{b}_{st}) \otimes \mathbf{q}(\boldsymbol{\eta}_{st}) \otimes \mathbf{q}_b^{st} \otimes \mathbf{q}_i^b \tag{19}$$

The star tracker parameters are summarized in Table 5.

Table 2. DSN Update

Parameter	3σ
Range Noise, m	25
Range-rate Noise, cm/s	1.5
Range Bias, m	25
Range-rate Bias, cm/s	1.5
Elevation Mask, deg	10.0
Max Pass Duration, hr	6.0

Table 3. Accelerometer[22]

Parameter	3σ
VRW, mm/s/sqrt(s)	0.3
Bias, μg	84
Scale Factor, ppm	450
Nonorthogonality, arcsec	17
Markov Bias, μg	84
Markov Scale Fact, ppm	450

Table 4. Gyros[22]

Parameter	3σ
ARW, deg/$\sqrt{hr}$	0.015
Bias, deg/hr	0.036
Scale Factor, ppm	27
Nonorthogonality, arcsec	19
Markov Bias, deg/hr	0.036
Markov Scale Factor, ppm	27

Table 5. Startracker[22]

Parameter	3σ
Boresight Noise, arcsec	72
Crs-Boresight Bias, arcsec	24
Misalignment, deg	0.5

Table 6. BLACMAGIC

Parameter	3σ
Version	v3.0
Tuning Date	2024
Gnd Stations	–

Table 7. Process Noise

Parameter	3σ
Trans (LEO)	(Table 11)
Trans (Cis-lunar)	(Table 11)
Rotational, rad/s/$\sqrt{s}$	$0.0e^{-6}$

Table 8. Initial Dispersions

Parameter	3σ
Position Axis, km	0.50
Velocity Axis, m/s	0.15
Attitude Axis, deg	0.9
Attitude-Rate, deg/s	0.0

Table 9. Initial Navigation

Parameter	3σ
Position Axis, km	0.20
Velocity Axis, m/s	0.05
Attitude Axis, deg	0.20
Attitude-Rate, deg/s	0.00

Table 10. Thrusters

Parameter	3σ
Bias, cm/s	0.5
Noise, cm/s	1.5
SF, ppm	6050
Misalign, deg	0.05

Translational Burn Modeling

All the major translational burns and the correction burns are assumed to be impulsive and are executed using a two-level targeter[23,24,25,26,27] (TLT) that targets the EI parameters and lunar radius

of periapses. The algorithm works by dividing the trajectory into segments or a series of intermediate targets known as patch states. The first stage, or the level-I process, introduces impulsive maneuvers at the interior patch states until position continuity across all segments is achieved. The second stage, or the level-II process, adjusts the shape of the trajectory by spatially and temporally relocating the patch states to drive the velocity discontinuities to zero. This approach is not limited to merely targeting a terminal position vector, but any terminal constraint such as flight path angle, altitude, velocity magnitude, or any function of the position and velocity state. All the impulsive burns have execution errors due to thruster misalignment, scale factor, bias, and noise. Table 10 lists each thruster error model component.

Disturbance Acceleration Modeling

Artemis II will be the first mission to have crew to fly the Orion spacecraft. As a result, their are additional disturbance accelerations due the Environmental Control and Life Support System (ECLSS) that provides clean air and water to the crew. The ECLSS perturbations include pressure swing absorption (PSA) during crew sleep, awake, and active periods, waste water vents, and ammonia sublimator. The non-ECLSS perturbations include attitude dead-banding maneuvers, attitude slew maneuvers, and solar radiation pressure. A summary of previously derived process noise values values[18] $\mathbf{Q}$ for Artemis II is provided below in Table 11.

Table 11. Artemis II ECLSS and Non-ECLSS Disturbance Accelerations

Event	**Process Noise**	**Q** (m^2/s^3)	**Duration**
ECLSS	Pressure Swing Adsorption (Sleep)	2.7740×10^{-9}	During sleep periods only
	Pressure Swing Adsorption (Awake)	8.7620×10^{-9}	During non-exercise awake periods
	Pressure Swing Adsorption (Active)	6.0146×10^{-8}	During crew exercise periods only
	Waste Water Vents	4.6030×10^{-8}	8.6 min, 4 times a day
	Ammonia Boiler	7.9421×10^{-6}	45 min, 1 hour prior EI
Non-ECLSS	Attitude Dead-banding Maneuvers	3.1883×10^{-14}	During entire on-orbit phase
	Attitude Slew Maneuvers	1.1262×10^{-11}	During entire on-orbit phase
	Solar Radiation Pressure	8.3338×10^{-15}	During entire on-orbit phase

A subtle yet important aspect of the ECLSS impact study is characterizing how the process noise reflecting the disturbance accelerations due to the ECLSS events are modeled. There are several options of modeling the disturbance accelerations due to venting highlighted in Figure 6. The first assumes a generic three-axis venting direction with the ECLSS disturbance accelerations averaged out over the entire profile such that a single process noise value is incorporated in all three body axes. The second also assumes a generic three axis direction with the ECLSS disturbance accelerations but they are scheduled at their specified time intervals. The third approach models a specific venting direction in the Orion structural frame at their specified time intervals which requires the Orion vehicle attitude to be defined throughout the entire scenario.

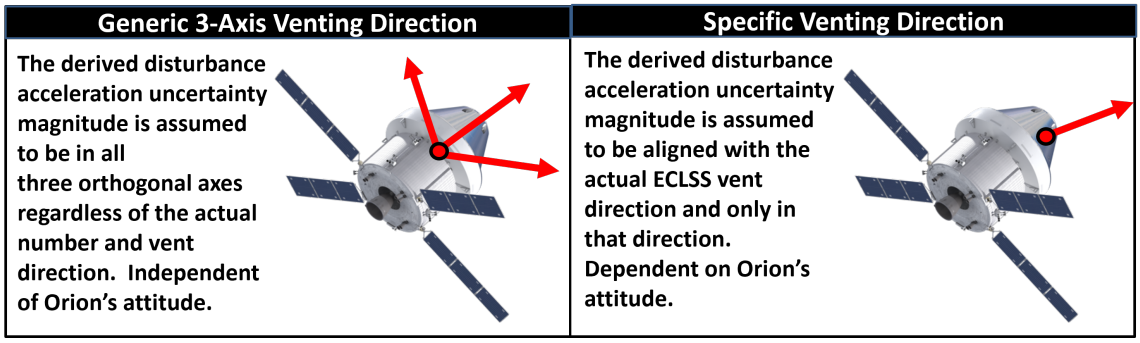

Figure 6. Artemis II Venting Modeling Approaches

For this analysis, since the vehicle orientation is not formally defined for the end-to-end mission yet, the ECLSS modeling adopts the second option such that the vehicle attitude profile does not impact the resulting disturbance accelerations due to venting, but the magnitude of the disturbance accelerations varies and is scheduled to reflect the frequency, number, and duration of each ECLSS event as outlined in Table 11. This approach is slightly conservative, but relevant.

SENSITIVITY TO GN&C SYSTEM USING BASELINE BURN PLACEMENT

To understand the impacts of the correction burn placement on the integrated GN&C performance, it is first instructional to understand the overall sensitivity to the GN&C system itself assuming the baseline Artemis II correction burn placement. This helps distinguish those impacts largely caused by the timing of the correction burns and those induced by the GN&C system (i.e. large navigation errors). The first set of analysis results highlight the impacts of different ground tracking navigation models starting with a higher fidelity and more accurate navigation performance to a lower fidelty with more conservative navigation uncertainty. After highlighting the impacts of different navigation models, the next set of figures provide insight of the sensitivity to the integrated GN&C performance due to initial conditions, disturbance accelerations, maneuver execution errors, and the navigation sensors.

The performance results for the baseline trajectory correction burn placement using DSN is provided in Figure 7. Figure 7(a) highlights details regarding the total delta-v (99.73%, top left plot) along with measurement scheduling, inertial position and velocity navigation errors, the reference trajectory with the simulated burn placement and crew sleep schedule, and the inertial position and velocity trajectory dispersions. Figure 7(b) summarizes the performance compliance with the top-level requirements defined previously which includes total delta-v dispersions and the entry interface requirements. When including three DSN and three NSN ground stations to support ranging and 3-way doppler, the entry interface conditions can be achieved with a minimum of 71% margin with a total delta-v of 5.6 m/s.

The integrated GN&C performance results using the BLACMAGIC model with the baseline correction burn placement are showin in Figure 8. Due to the resulting degraded navigation performance with this lower-fidelity model, the EI percent margin decreased to 69% with an increase of total delta-v to 7.2 m/s. Using the most conservative navigation model with the pregenerated covariance matrices, the resulting performance is summarized in Figure 9. Now the worst entry interface percent margin is down to 1% and the total total delta-v has doubled to 15.7 m/s.

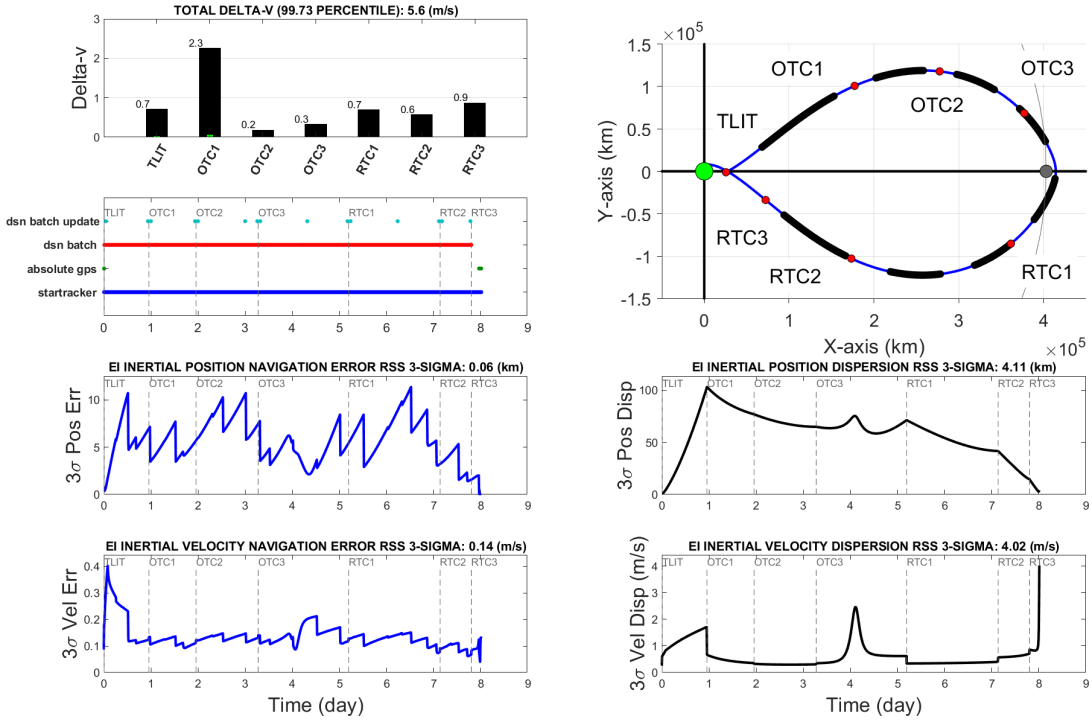

(a) Overview of Artemis II Trajectory Performance Using DSN Ground Navigation

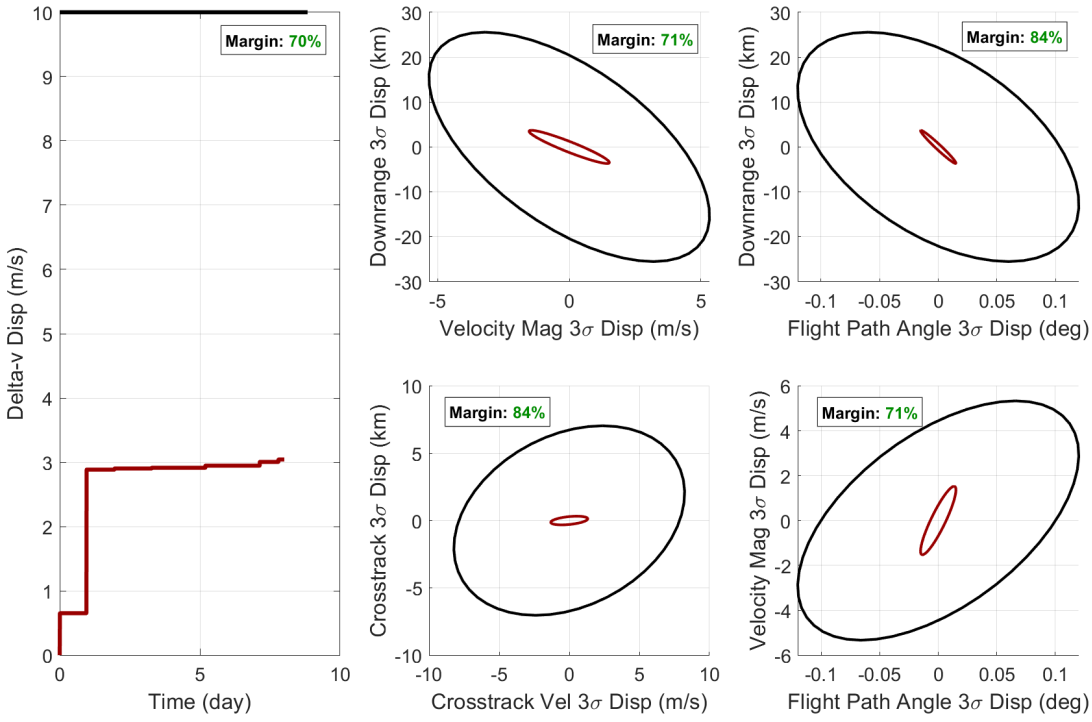

(b) Delta-v and Entry Interface Requirement Compliance Using DSN Ground Navigation

Figure 7. Performance Using DSN Navigation Model with Baseline Burn Placement

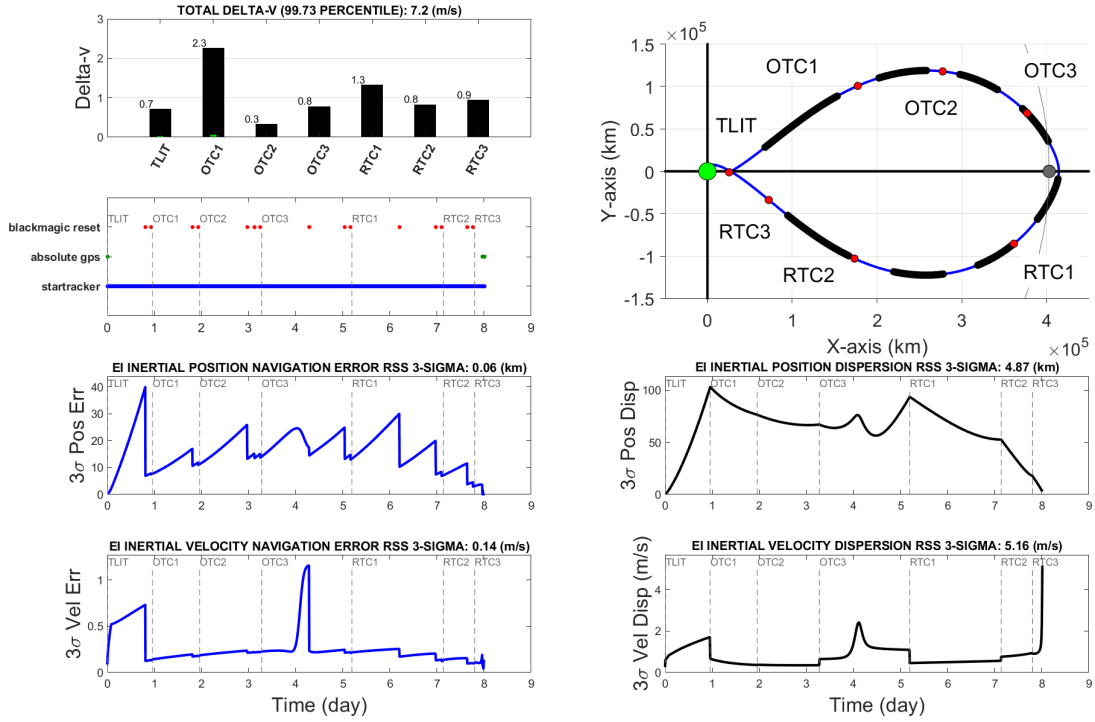

(a) Overview of Artemis II Trajectory Performance Using BLACMAGIC Ground Navigation

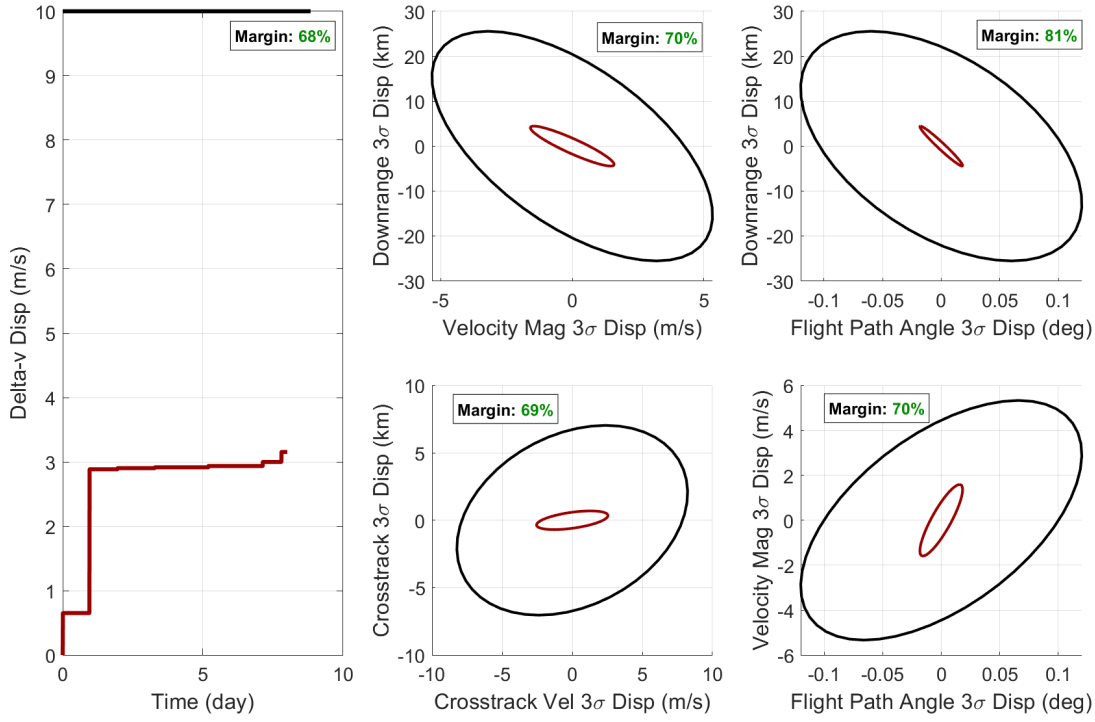

(b) Delta-v and Entry Interface Requirement Compliance Using BLACMAGIC Ground Navigation

Figure 8. Performance Using BLACMAGIC Navigation Model with Baseline Burn Placement

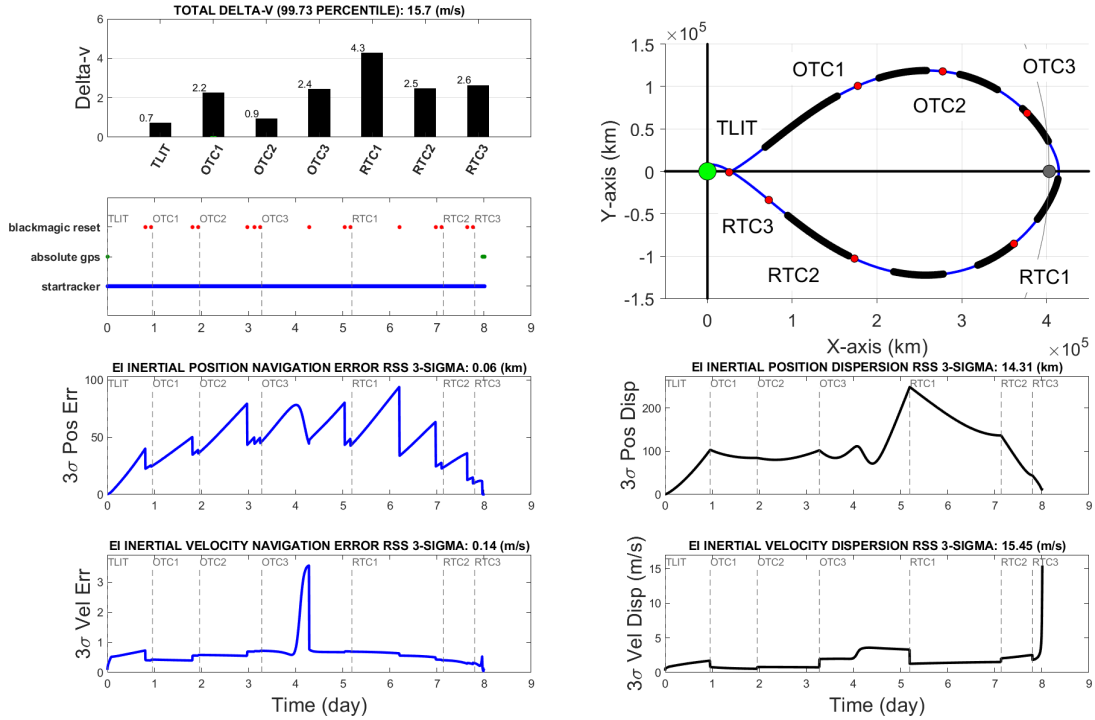

(a) Overview of Artemis II Trajectory Performance Using Pregenerated Ground Navigation

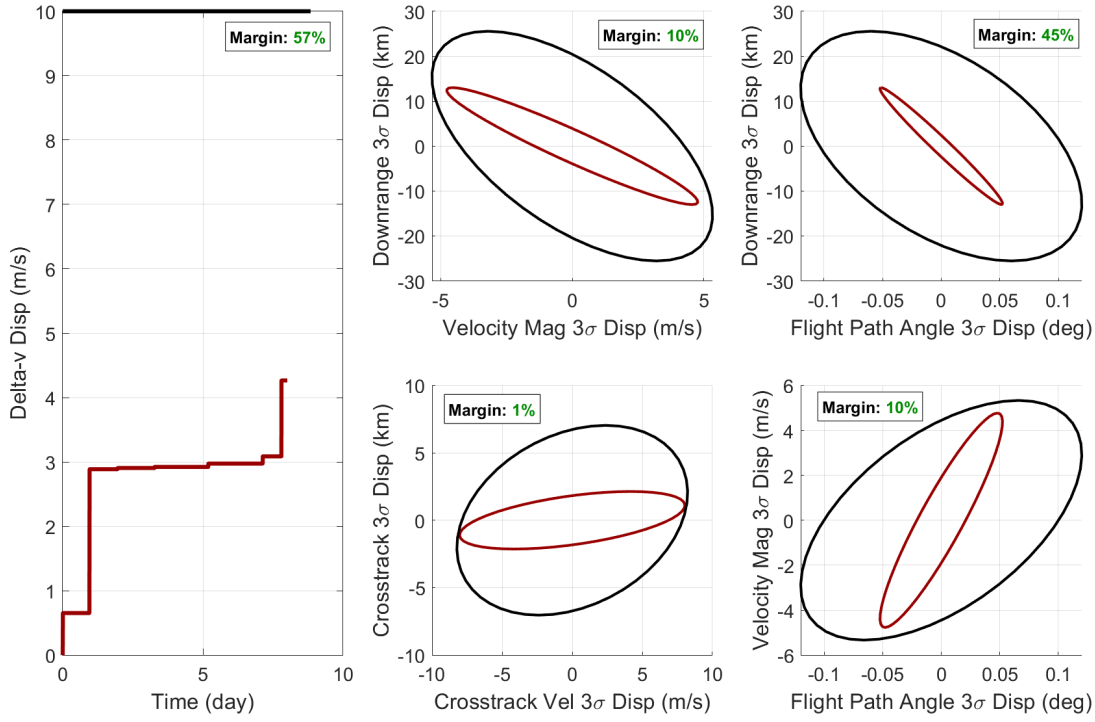

(b) Delta-v and Entry Interface Requirement Compliance Using Pregenerated Ground Navigation

Figure 9. Performance Using Pregenerated Navigation Model with Baseline Burn Placement

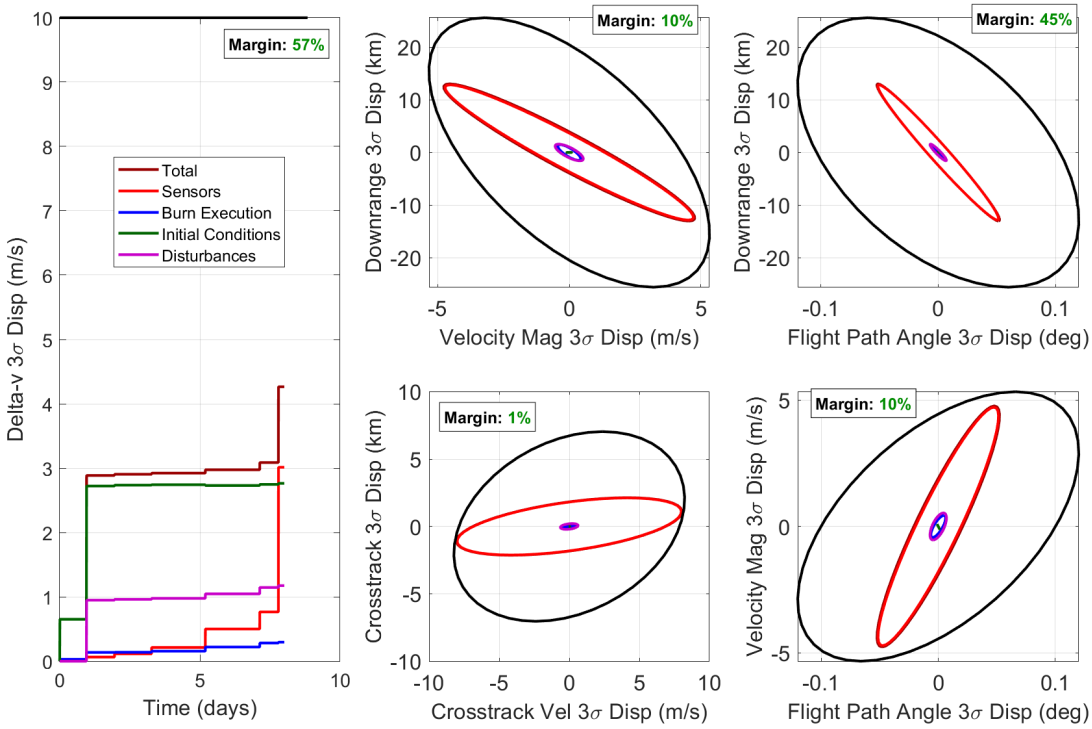

(a) Delta-v and Entry Interface Requirement Compliance Sensitivity

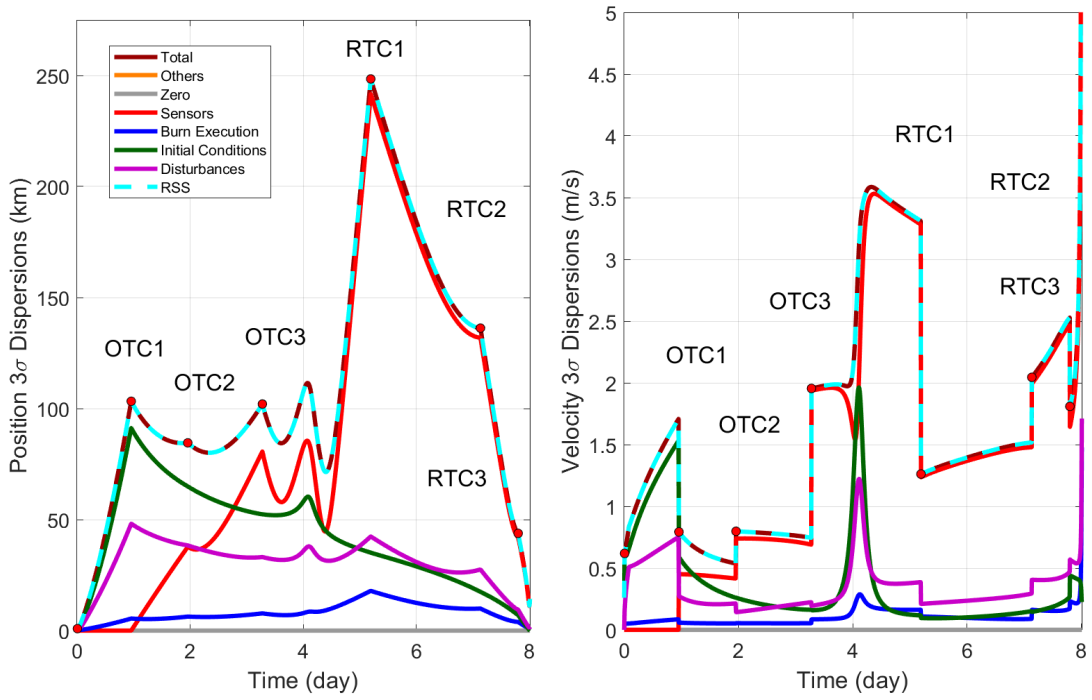

(b) Position Disperions Sensitivity

(c) Velocity Disperions Sensitivity

Figure 10. Impacts of Artemis II Correction Burn Placement to Integrated GN&C Performance

This sensitivity to the navigation system model and other GN&C system parameters such as venting disturbances, maneuver execution error, and initial conditions are shown in Figure 10. The sensitivity to delta-v and the entry interface dispersions are shown in Figure 10(a) where the time history sensitivity results for the inertial position and velocity dispersions are provided Figure 10(b) Figure 10(c) respectively. The dominant factor for these major performance metrics is the navigation or the GSU accuracy. For delta-v, the next major contributor is initial condition uncertainty. By either improving the ground tracking system or the post-TLI initial dispersions, these two factors can improve the integrated GN&C performance the most given the baseline trajectory correction burn placements are fixed.

SENSITIVITY TO ALTERNATE ARTEMIS II CORRECTION BURN PLACEMENT

Given the sensitivity to these performance metrics with respect to the GN&C system, the foundation is set to investigate the sensitivity to the actual placement of each of the trajectory correction burns. The sensitivity results are grouped according to the outbound segment of the trajectory or the return phase. For example, Figure 11 and Figure 12 capture the impacts of altering the outbound correction burns while Figure 13 and 14 capture the trends of the return trajectory correction burns. In addition to seeing the impacts of moving the correction burn time when all the other correction burns still occur, sensitivity results are also generated in cases when it is the last burn, representing a free-drift condition.

All the correction burns from OTC1 to RTC3 are moved at equal intervals over the crew day in which they occur. For example, since OTC1 occurs near the middle of Crew Day 4, the OTC1 burn is moved at about one-hour intervals from 5 hours prior to 5 hours after the nominal burn time as illustrated in Figure 11(b) and Figure 11(a). Each interval is marked with a solid circle as shown in Figure 11(a) to illustrate the location or placement of the burn that is evaluated in context of the trajectory profile. Burns that occur earlier are marked with blue and corrections that occur later progress to an orange filling. The baseline burn epoch is indicated either with the larger solid yellow or red dot.

The mapping of the total delta-v and the percent margin of the EI dispersions as a function of the correction burn time constitute a *mission map*. Figure 11(b), for example, represents the mission map for OTC1. The solid black lines represents the total delta-v and the colored lines represent one of the four entry interface requirements. The dotted blue line represents the velocity magnitude and downrange position dispersions (EI1). The dotted dashed cyan color reflects the flight path angle versus downrange dispersion requirement (EI2). The solid green line corresponds to the cross-track position and velocity dispersions (EI3) and the dashed red line shows the flight path angle versus velocity magnitude (EI4).

Sensitivity to Outbound Trajectory Correction Burn Placement

There are several key observations to extract from Figure 11 that shows the sensitivity to different outbound burn placements for OTC1, OTC2, and OTC3. When all the correction burns are performed, the burn time of each has little impact on the entry interface dispersion margin. It is clear that the EI performance metric that is most stringent is satisfying the cross-track position and velocity (EI3, solid green line). The performance metric with the greatest margin is the EI velocity magnitude and downrange position constraint (EI1, dotted blue line).

In terms of total delta-v, there are several expected and unexpected trends. For OTC1 in Figure

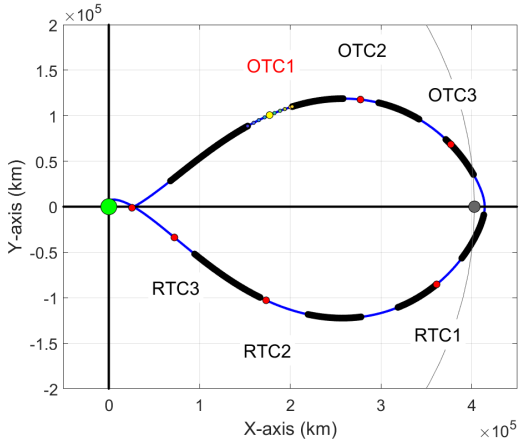

(a) OTC1: Trajectory with all burns

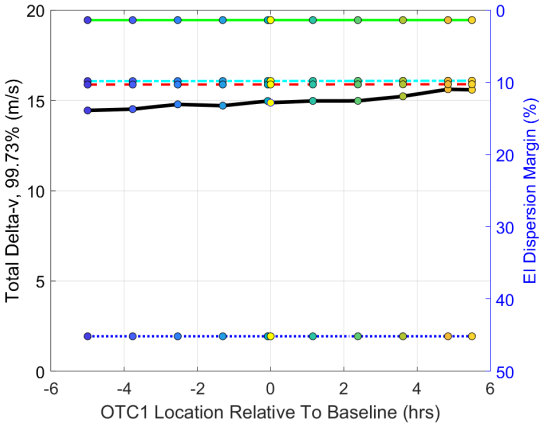

(b) OTC1: Mission Map with all burns

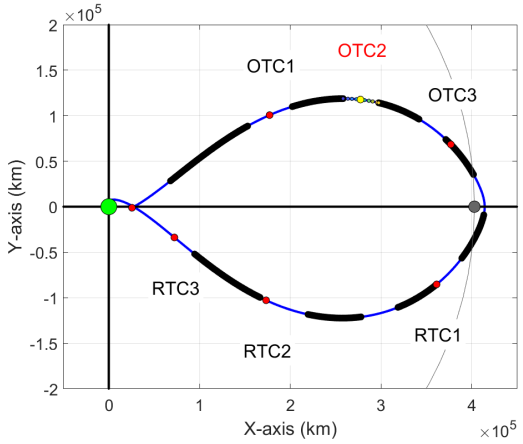

(c) OTC2: Trajectory with all burns

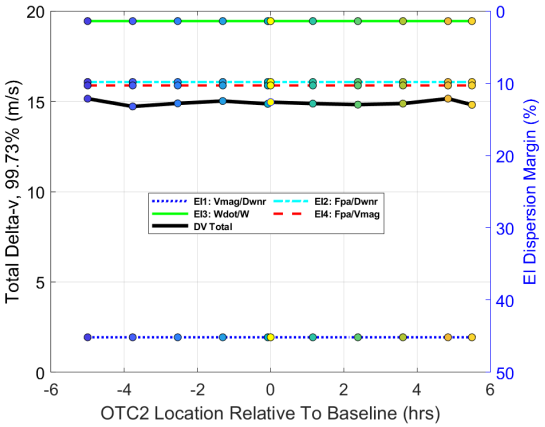

(d) OTC2: Mission Map with all burns

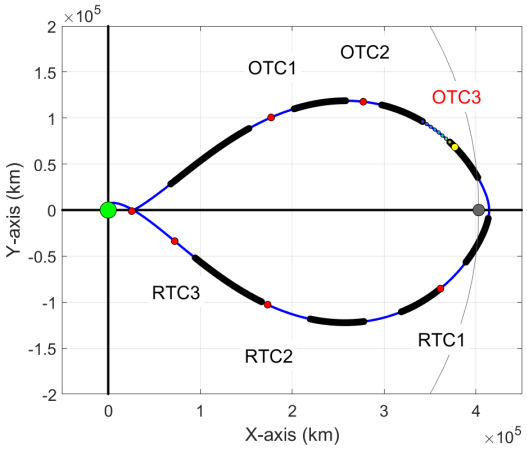

(e) OTC3: Trajectory with all burns

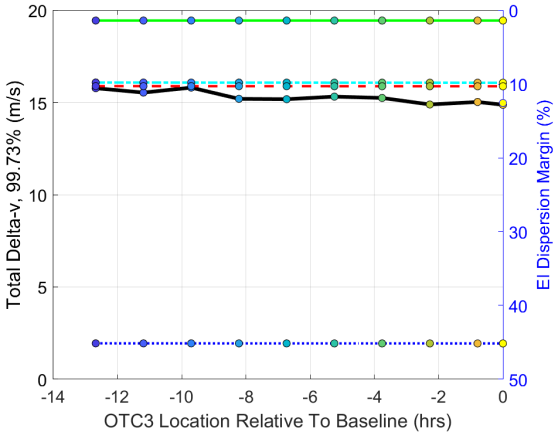

(f) OTC3: Mission Map with all burns

Figure 11. Outbound Mission Maps with All Correction Burns

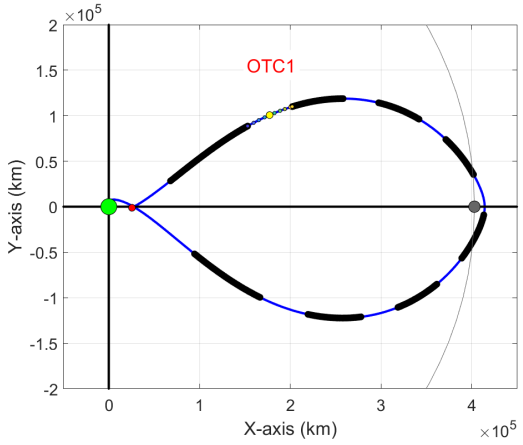

(a) OTC1: Trajectory with all burns

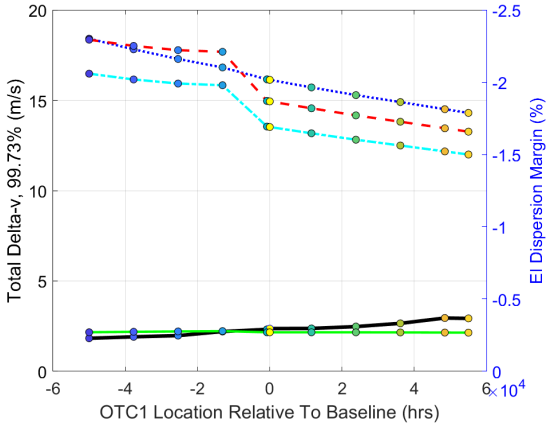

(b) OTC1: Mission Map with all burns

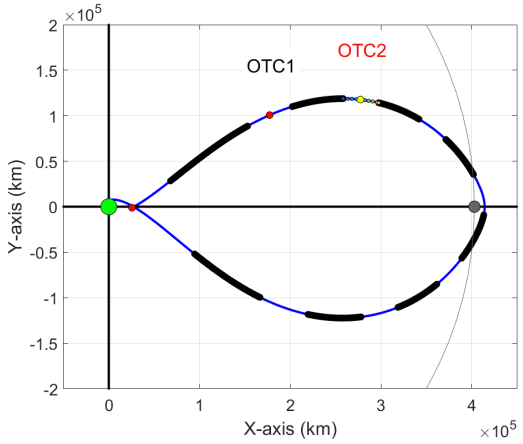

(c) OTC2: Trajectory with free-drift

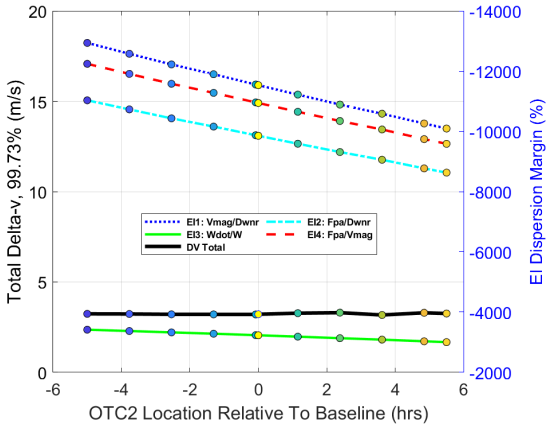

(d) OTC2: Mission Map with free-drift

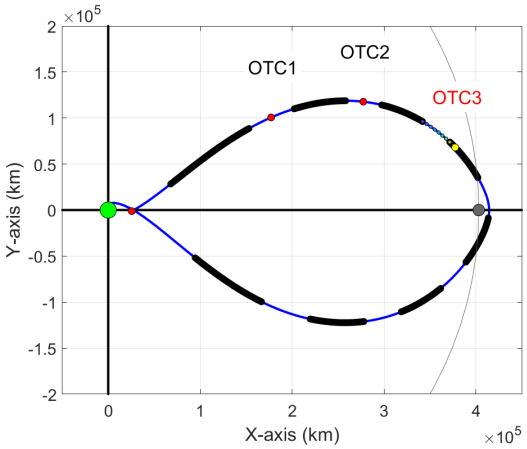

(e) OTC3: Trajectory with optmized burn

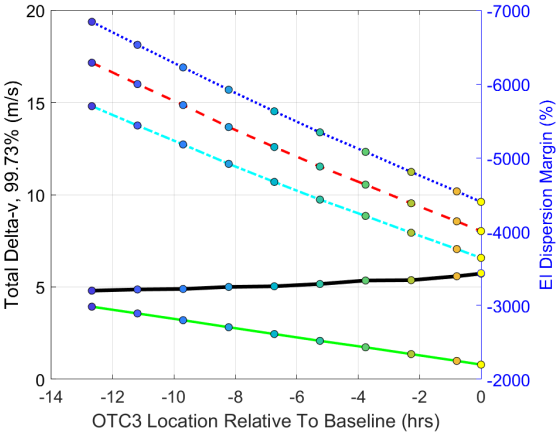

(f) OTC3: EI with optimized burn

Figure 12. Outbound Mission Maps with Free-Drift

11(b), total delta-v is reduced by executing it as early as possible and is maximized the later it is performed in the crew day. This is a general pattern to be expected. For longer post-burn coasting arcs, less delta-v is required. About 1 m/s differential is observed between the *best* and *worst* OTC1 times. For OTC2 in Figure 11(d), the total delta-v has little variation due to its placement and is largely insensitive to when it is performed. However, for OTC3 in Figure 11(f), total delta-v can be reduced by waiting towards the end of the crew day. Again, the amount is not significant, but on the order of about 1 m/s. This unanticipated trend may be due to the impacts of being in the vicinity of the moon.

In the unanticipated event of a free-drift condition where a specific OTC burn is the last burn, its direct impact on entry interface dispersions becomes more dramatic and the sensitivities more pronounced as shown in Figure 12. The first key trend for EI conditions is one that is expected. The longer the correction burn is delayed and/or the more correction burns performed, the greater the reduction in EI dispersions. This is apparent for each outbound correction burn in Figure 12(b), Figure 12(d), and Figure 12(f) respectively. Similarly, the greater reduction in EI dispersions by delaying the correction burns to have shorter post-burn coasting arcs (or doing more of them) comes at the cost of an increase in total delta-v. This common trade between these two naturally opposing performance metrics becomes the ultimate trade mission operators must identify and select.

Sensitivity to Return Trajectory Correction Burn Placement

The mission maps for the return trajectory correction burns in Figure 13 and Figure 14 reveal some differing trends than those observed for the outbound correction burns. When all the correction burns are performed, there is little sensitivity to the RTC1 placement in terms of EI performance and minimal variation in total delta-v as shown in Figure 13(b). However, with RTC2 and RTC3 the sensitivity to EI dispersions with the burn placements becomes more pronounced as Orion arrives closer to Earth. For RTC2 in Figure 13(d), the cross-track position and velocity dispersions have a noticeable increase as RTC2 is delayed. In fact, in order to have a positive margin it must be delayed toward the end of the crew day.

By the last crew day when RTC3 is performed in Figure 13(f) the opposite trend emerges where if it is delayed too long, EI requirements cannot be satisfied, particularly for the cross-track position and velocity constraints (EI3, solid green line). Despite the degradation in cross-track, delaying improves the other EI constraints. The one expected trend observed for the return correction burns is that when the burns are delayed, the total delta-v increases. In other words, executing the return trajectory correction burns earlier in the day has the potential to reduce total potential delta-v.

To pronounce the impact of the return trajectory correction burn placement, Figure 14 emphasizes the EI performance when some of the correction burns are removed, particularly those following a particular burn of interest. For example, Figure 14(b) shows the EI sensitivity to RTC1 burn placement. Similar to the RTC2 placement in Figure 14(d) the unexpected trend of an increasing cross-track position and velocity dispersions (EI3, solid green line) as the correction burns are performed later in the crew day. For all the other EI metrics, they are reduced as RTC1 and RTC2 are delayed. The mission map for RTC3 in Figure 14(f) is rather unique. The only previous correction burn assumed is OTC1. In this instance, EI performance is always enhanced by executing RTC3 as early as possible in the crew day. Both EI and total delta-v performance metrics are enhanced by an earlier correction burn time.

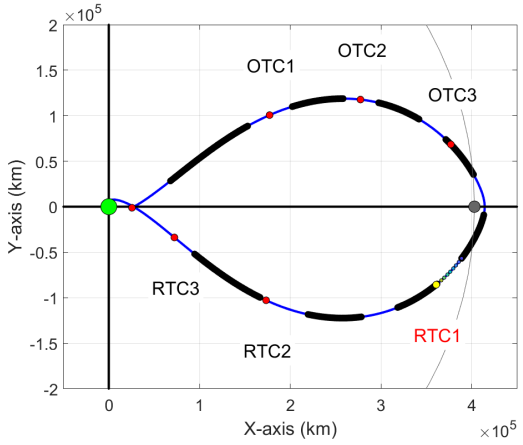

(a) RTC1: Trajectory with all burns

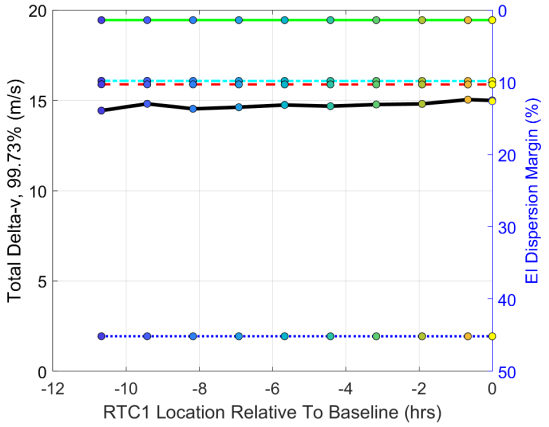

(b) RTC1: Mission Map with all burns

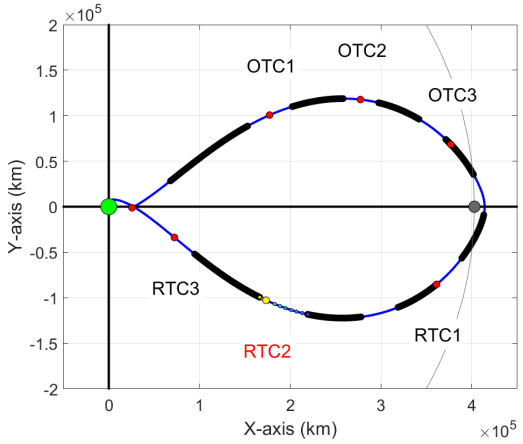

(c) RTC2: Trajectory with all burns

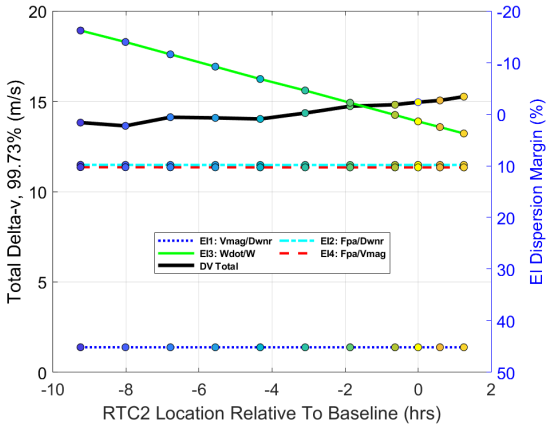

(d) RTC2: Mission Map with all burns

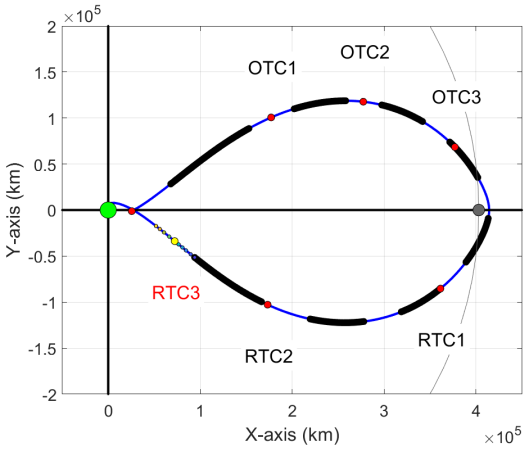

(e) RTC3: Trajectory with all burns

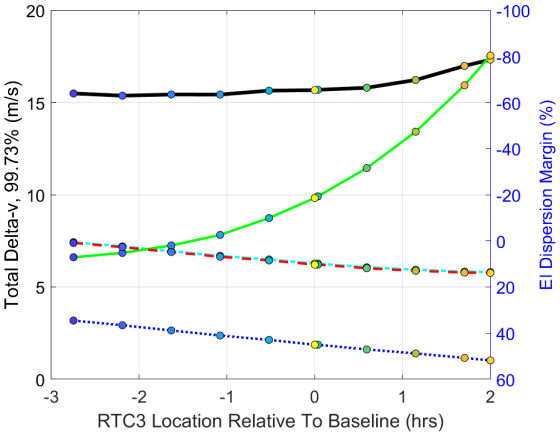

(f) RTC3: Mission Map with all burns

Figure 13. Return Mission Maps with All Correction Burns

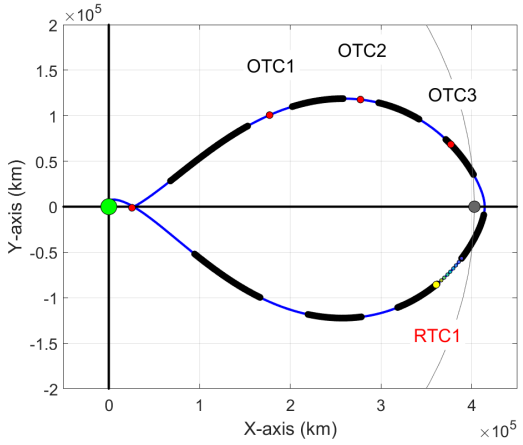

(a) RTC1: Trajectory with free-drift

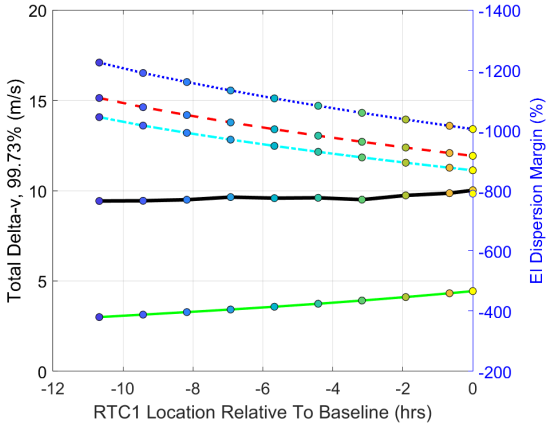

(b) RTC1: Mission Map with free-drift

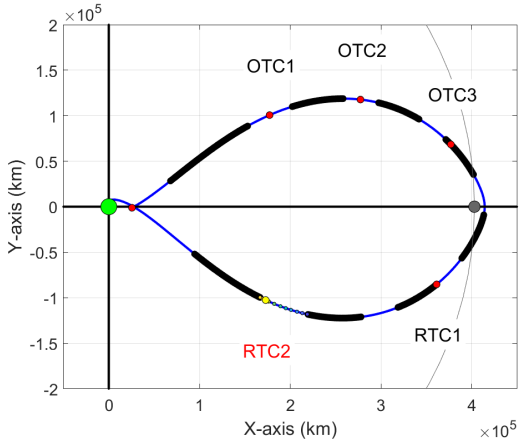

(c) RTC2: Trajectory with free-drift

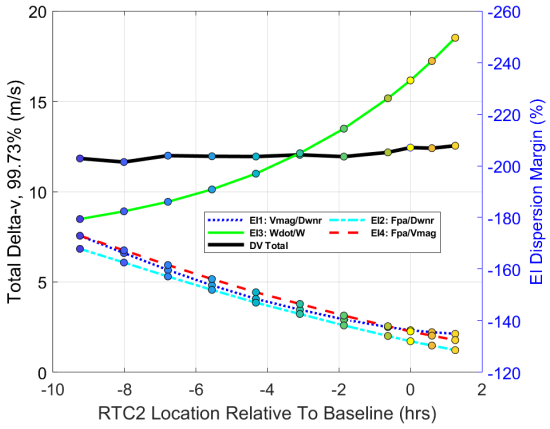

(d) RTC2: Mission Map with free-drift

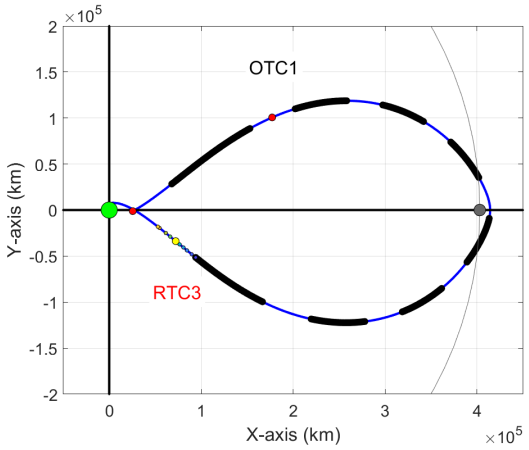

(e) RTC3: Trajectory with free-drift

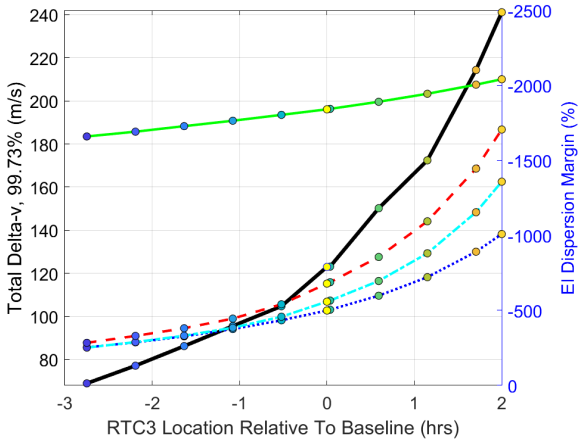

(f) RTC3: Mission Map with free-drift

Figure 14. Return Mission Maps with Free-Drift

Sensitivity to Optimization Artemis II Correction Burn Placement

The mission maps highlighting the sensitivity of key performance metrics provide critical insight in determining the *optimal* placement of the correction burns. To demonstrate how this process can occur not only using a variety of optimization algorithms, but how a portion can be done manually by mission planners and flight controllers, a simple but relevant Artemis II optimization problem is formulated. The question to answer is to optimize the placement of the RTC3 that minimizes the entry interface dispersions while not exceeding a total delta-v threshold of 20 m/s.

Given the sensitivity data in Figure 14(f), it is organized in Figure15(a) with the total delta-v (solid black line), the EI percent margin average (solid blue line), and the minimum EI percent margin (solid red line). If the objective function is to maximize the EI percent margin average (solid blue line) then the optimal burn time for RTC3 (indicated with a solid blue circle) is about an hour prior to the current baseline time (indicated with a solid yellow circle), as shown in Figure 15. Not only are the EI dispersions reduced but the total delta-v is slightly less too. If the objective function was to maximize the minimum EI percent margin (solid red line), then the optimized RTC3 burn placement is over 2 hours prior to the baseline RTC3 time. This optimized location is indicated with a solid green circle. These key trends not only become intuitive for mission planners and trajectory operators, they can also be utilized in more complex trajectory optimization algorithms to solve the entire correction burn placement simultaneously.

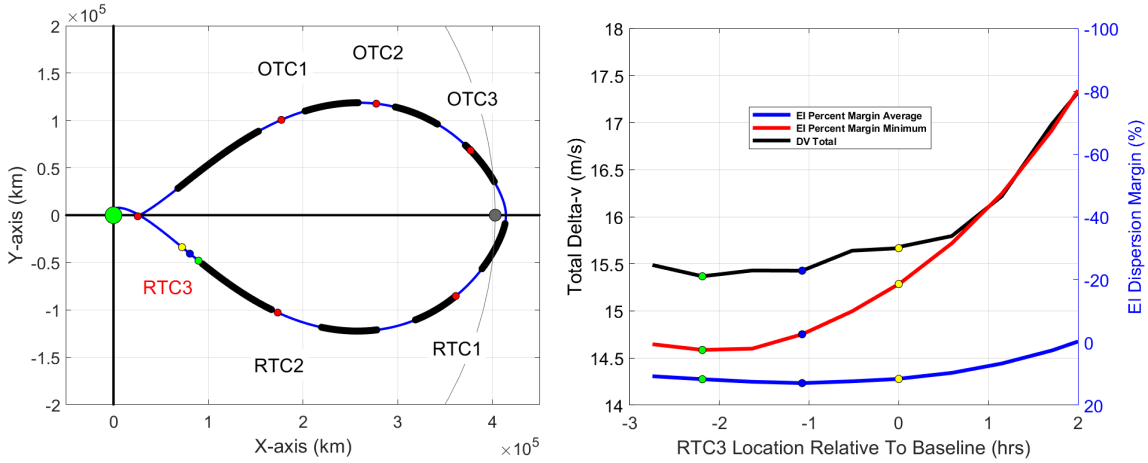

(a) RTC3: Trajectory with All Burns

(b) RTC3: Mission Map with free-drift

Figure 15. Optimization of RTC3 Burn Placement Using Mission Map Data

CONCLUSION

This work provides preliminary performance results that seek to identify optimized trajectory correction burn placement for the upcoming NASA Artemis II mission by generating the sensitivity of key integrated GN&C performance metrics to the placement of these small but essential translational burns. This analysis capability was demonstrated for the free-return profile, but it exists for all future Artemis missions too. The trends that emerge provide mission planners and trajectory operators intuitive information that allows them to instinctively identify *optimal* burn times in context of an assortment of competing mission criteria and priorities. As was observed, sometimes

burn placement matters. Oftentimes it does not. This technique can quickly and reliably (without requiring long Monte Carlo analysis runs) identify the correction burns that have impact and supply data to inform wise decisions that mission planners and operators must make. In many instances, it merely confirms their natural intuition but it also provides a rapid approach to correct faulty assumptions that may mislead to detrimental conclusions or deserves further investigation. It helps to strategically identify focus areas to reduce risk to mission success given limited assets and resources.

This same sensitivity data can also be incorporated into trajectory optimization algorithms to solve more complex trades that inevitably emerge when supporting flight and potential contingencies that may arise. By integrating linear covariance analysis with optimization techniques, uncertainty in the system can be accommodated and trajectory correction burns which are nominally zero, can be strategically placed to reduce total delta-v (nominal + 3-sigma dispersions) while ensuring the vehicle satisfies entry interface dispersion requirements. Arbitrarily selecting the number and placement of the trajectory correction burns following the trans-lunar injection burn can lead to a noticeable increase of delta-v and violation of entry interface requirements. The sensitivity to burn placement as a function of the navigation system and the selected optimization objective functions is also provided.

ACKNOWLEDGMENTS

The authors express appreciation to Collin York, Chris Spreen, Matt Gualdoni, Brandon Wood, Ian Dux, Randy Eckman, and others who enabled the Artemis II scenario development that enhanced this research effort.

REFERENCES

[1] P. S. Maybeck, *Stochastic models, estimation, and control*, Vol. 1. New York: Academic Press, 1979.

[2] D. K. Geller, "Linear Covariance Techniques for Orbital Rendezvous Analysis and Autonomous Onboard Mission Planning," *Journal of Guidance, Control, and Dynamics*, Vol. 29, November-December 2006, pp. 1404–1414.

[3] D. Woffinden, R. Eckman, and S. Robinson, "Optimized Trajectory Correction Burn Placement for the NASA Artemis II Mission," Breckenridge, CO, AAS 23-062, 1 Feb - 6 Feb 2023.

[4] K. Jin, D. K. Geller, and J. Luo, "Robust Trajectory Design for Rendezvous and Proximity Operations with Uncertainties," *Journal of Guidance, Control, and Dynamics*, Vol. 43, No. 4, 2020, pp. 741–753.

[5] D. K. Geller, S. Shuster, D. Woffinden, and S. Bieniawski, "Robust Cislunar Trajectory Optimization via Midcourse Correction and Optical Navigation Scheduling," *44th Annual AAS Guidance, Navigaiton and Control Conference*, Breckenridge, CO, AAS 22-065, 4-9 February 2022 2022.

[6] T. Goulet, D. Woffinden, N. Collins, and B. Andrews, "Robust Trajectory Design for Rendezvous in a Near Rectilinear Halo Orbit," *45th Rocky Mountain AAS GN&C Conference*, Breckenridge, CO, AAS 23-066, 2 Feb - 8 Feb 2023.

[7] G. Calkins, D. Woffinden, and Z. Putnam, "Robust Trajectory Optimization for Guided Powered Descent and Landing," *2022 AAS/AIAA Astrodynamics Specialist Conference*, Charlotte, NC, AAS 22-660, 7-11 August 2022 2022.

[8] J. Joshi, D. Woffinden, and Z. Putnam, "End-to-End Mars Aerocapture Analysis Using Linear Covariance Techniques and Robust Trajectory Optimization," *2022 AAS/AIAA Astrodynamics Specialist Conference*, Charlotte, NC, AAS 22-678, 7-11 August 2022 2022.

[9] D. Woffinden, S. Shuster, and S. Geller, David Kand Bieniawski, "Robust Trajectory Optimization and GN&C Performance Analysis For NRHO Rendezvous," *2022 AAS/AIAA Astrodynamics Specialist Conference*, Charlotte, North Carolina, 22-564, 7-11 August 2022 2022.

[10] D. Geller, D. Woffinden, and S. Bieniawski, "Sensitivity of Optimal Midcourse Correction Scheduling for Robust Cislunar Trajectory Design," *45th Rocky Mountain AAS GN&C Conference*, Breckenridge, CO, AAS 23-061, 2 Feb - 8 Feb 2023.

[11] T. J. Moesser and D. K. Geller, "Guidance and Navigation Linear Covariance Analysis for Lunar Powered Descent," *AAS/AIAA Astrodynamics Specialist Conference*, Mackinac Island, Michigan, AAS 07-313, 19-23 August 2007.

[12] D. Geller and D. Christensen, "Linear Covariance Analysis for Powered Lunar Descent and Landing," *The Journal of Spacecraft and Rockets*, Vol. 46, Nov-Dec 2009, pp. 1231–1248.

[13] D. Woffinden, S. Robinson, J. Williams, and Z. Putnam, "Linear Covariance Analysis Techniques to Generate Navigation and Sensor Requirements for the Safe and Precise Landing - Integrated Capabilities Evolution (SPLICE) Project," *AIAA Scitech 2019 Forum*, San Diego, CA, AIAA 2019-0662, 7-11 January 2019 2019.

[14] J. W. Williams, W. E. Brandenburg, D. C. Woffinden, and Z. R. Putnam, "Validation of Linear Covariance Techniques for Mars Entry, Descent, and Landing Guidance and Navigaiton Performance Analysis," *AIAA Scitech 2022 Forum*, 2022.

[15] J. Rea, "Entry Interface Accuracy Requirements for Exploration Mission Critical Design Review," Tech. Rep. FltDyn-CEV-15-28, National Aeronatuics and Space Administration, Johnson Space Center, Engineering Directorate, July 2015.

[16] R. Zanetti and C. DSouza, "Navigation and Dispersion Analysis of the First Orion Exploration Mission," *39th Annual AAS Guidance and Control Conference*, Breckenridge, CO, AAS 15-758, 5-10 Feb 2015.

[17] C. DSouza, G. Holt, R. Zanetti, and B. Wood, "Ground-Based Navigation and Dispersion Analysis for the Orion Exploration Mission 1," *39th Annual AAS Guidance and Control Conference*, Breckenridge, CO, AAS 16-235, 5-10 Feb 2016.

[18] C. D'Souza and R. Zanetti, "Navigation Design and Analysis for the Orion Exploration Mission 2," *AAS/AIAA Astrodynamics Specialist Conference*, Stevenson, WA, AAS 17-643, 20-24 Aug 2017.

[19] B. C. Collicott and D. C. Woffinden, *Lunar Navigation Performance using the Deep Space Network and Terrain Relative Navigation to Support Precision Landing*. 19-21 January 2021.

[20] D. Woffinden, D. Roth, J. Orphee, and B. Young, "An Orbit Determination Comparison Study and Demonstration for Rendezvous and Docking in a Near Rectilinear Halo Orbit from the Lunar Surface," *AAS/AIAA Astrodynamics Specialist Conference*, Broomfield, Colorado, 11-15 August, 2024. AAS 24-337.

[21] K. Ward, C. D'Souza, and G. Holt, "Grimorium Verum: On the Practice of BLACMAGIC for Simnulation of Ground Tracking Performance in Orion GN&C Testing," *AAS/AIAA Astrodynamics Specialist Conference*, Broomfield, Colorado, 11-15 August, 2024. AAS 24-243.

[22] A. M. Dwyer-Cianciolo, C. D. Karlgaard, D. Woffinden, R. A. Lugo, J. Tynis, R. R. Sostaric, S. Striepe, R. Powell, and J. M. Carson, "Defining Navigation Requirements for Future Missions," *AIAA Scitech 2019 Forum*, San Diego, 2019. 2019-0661.

[23] B. G. Marchand, K. Howell, and R. Wilson, "Improved Corrections process for Constrained Trajectory Design in the n Body Problem," *Journal of Spacecraft and Rockets*, Vol. 35, July 2007, pp. 1–33.

[24] M. W. Weeks, B. G. Marchand, C. W. smith, and S. Scarritt, "Design of the Onboard Autonomous Targeting Algorithm for the Trans-Earth Phase of Orion," Honolulu, Hawaii, AIAA Guidance, Navigation and Control Conference and Exhibit, 18-21 August 2008.

[25] B. G. Marchand, M. W. Weeks, C. W. Smith, and S. Scarritt, "Onboard Autonoous Targeting for the Trans-Earth Phase of Orion," *Journal of Guidance, Control, and Dynamics*, Vol. 33, May-June 2010, pp. 943–956.

[26] S. Scarritt, B. G. Marchand, A. J. Brown, W. H. Tracy, and M. W. Weeks, "Finite-Burn Linear Targeting Algorithm for Autonomous Path Planning Guidance," *Journal of Guidance, Control, and Dynamics*, Vol. 35, September-October 2012, pp. 1605–1615.

[27] S. K. Scarritt, T. Fill, and S. Robinson, "Advances in Orion's On-Orbit Guidance and Targeting System Architecture," Breckenridge, CO, AAS 15-096, 1 Feb - 6 Feb 2015.

[28] M. Mitchell, *An Introduction to Genetic Algorithms*. 1996.

[29] D. Woffinden, S. Bhatt, D. Kirkpatrick, and P. Spanos, "Optimal Multi-Variable Multi-Constraint Spacecraft GN&C Requirement Derivation," *41st Annual AAS Guidance and Control Conference*, Breckenridge, CO, AAS 18-095, 5-10 Feb 2018.